Distinct metabolic programmes established in the thymus control effector functions of γδ T cell subsets in tumour microenvironments

Noella Lopes[1,8], Claire McIntyre[2,8], Stefania Martin[3,8], Mathilde Raverdeau[4,8], Nital Sumaria[3], Ayano C. Kohlgruber[2], Gina J. Fiala[1], Leandro Agudelo[5], Lydia Dyck[4], Harry Kane[2,4], Aaron Douglas[4], Stephen Cunningham[4], Hannah Prendeville[4], Roisin Loftus[4], Colleen Carmody[2], Philippe Pierre[5,6], Manolis Kellis[7], Michael Brenner[2], Rafael J. Argüello[5], Bruno Silva-Santos[1,9], Daniel J. Pennington[3,9] and Lydia Lynch[2,4,9]

[1]Instituto de Medicina Molecular João Lobo Antunes, Faculdade de Medicina, Universidade de Lisboa, Lisbon, Portugal.

[2]Brigham and Women's Hospital, Harvard Medical School, Boston MA, USA.

[3]Blizard Institute, Barts and The London School of Medicine, Queen Mary University of London, London, E1 2AT, UK.

[4]Trinity Biomedical Science Institute, Trinity College Dublin, Dublin, Ireland.

[5]Aix Marseille Université, CNRS, INSERM, CIML, Centre d'Immunologie de Marseille-Luminy, Marseille, France.

[6]Institute for Research in Biomedicine (iBiMED) and Ilidio Pinho Foundation, Department of Medical Sciences, University of Aveiro, 3810-193 Aveiro, Portugal.

[7]MIT Computer Science and Artificial Intelligence Laboratory, MA, USA.

[8] and [9] These authors contributed equally to this work.

Correspondence should be addressed to D.J.P. (d.pennington@qmul.ac.uk).

Abstract

Metabolic programming controls immune cell lineages and functions, but little is known about γδ T cell metabolism. Here, we found that γδ T cell subsets making either IFN-γ or IL-17 have intrinsically distinct metabolic requirements. Whereas IFN-γ^+ γδ T cells were almost exclusively dependent on glycolysis, IL-17^+ γδ T cells strongly engaged oxidative metabolism, with increased mitochondrial mass and activity. These distinct metabolic signatures were surprisingly imprinted early during thymic development, and were stably maintained in the periphery and within tumours. Moreover, pro-tumoural IL-17^+ γδ T cells selectively showed high lipid uptake and intracellular lipid storage, and were expanded in obesity, and in tumours of obese mice. Conversely, glucose supplementation enhanced the anti-tumour functions of IFN-γ^+ γδ T cells and reduced tumour growth upon adoptive transfer. These findings have important implications for the differentiation of effector γδ T cells and their manipulation in cancer immunotherapy.

Introduction

T cells engage specific metabolic pathways to support their differentiation, proliferation and function[1,2]. Whereas naive αβ T cells oxidize glucose-derived pyruvate *via* oxidative phosphorylation (OXPHOS) or fatty acid oxidation (FAO) to generate ATP, most effector αβ T cells engage in aerobic glycolysis ("Warburg effect"), i.e. the conversion of glucose to lactate, to strengthen cell growth and proliferation[3]. On the other hand, while aerobic glycolysis is required for optimal αβ T cell effector function[4,5], tumour cells heavily consume glucose in the tumour microenvironment (TME), which has a dramatic impact on cytokine production by T cells and hampers tumour immunity[5,6]. There is therefore great interest in understanding how metabolism-based interventions could inhibit tumour metabolism while promoting effective anti-tumour immunity for improved immunotherapeutic outcomes[7].

γδ T cells represent a promising immune population for next-generation cancer immunotherapies[8,9]. Since they are not MHC-restricted nor dependent on neoantigen recognition, γδ T cells constitute a complementary layer of anti-tumour immunity to their αβ T cell counterparts[10]. In fact, many properties of γδ T cells, including sensing of "stress-inducible" changes and very rapid effector responses, align best with innate immunity, or "lymphoid stress-surveillance"[11], although in some instances they display adaptive-like behaviour and profound shaping of T cell receptor (TCR) repertoires[12,13].

The effector functions of murine γδ T cells are dominated by the production of two key cytokines, interleukin 17A (IL-17) and interferon-γ (IFN-γ). Beyond contributions to immune responses against pathogens, the provision of these two cytokines by γδ T cells is important in many (patho)physiological contexts, such as maintenance of tissue homeostasis[14,15,] autoimmunity[16] and cancer[8]. IL-17 and IFN-γ are mostly produced by distinct γδ T cell subsets that, unlike their $CD4^+$ T cell counterparts, typically acquire their effector functions during thymic development[17,18]. Thus, we and others have shown that thymic γδ T cell progenitors, driven by signals including those stemming from the TCR, split into a $CD27^+$ (and $CD45RB^+$) branch that makes IFN-γ but not IL-17; and a $CD27^-$ (and $CD44^{hi}$) pathway that selectively expresses IL-17[17-21].

The IFN-γ/IL-17 dichotomy between effector γδ T cell subsets is particularly relevant in cancer, since IFN-γ-producing γδ T cells ($\gamma\delta^{IFN}$) are associated with tumour surveillance and regression, whereas IL-17-secreting γδ T cells ($\gamma\delta^{17}$) promote primary tumour growth and metastasis, both in mice and in humans[8,22]. However, the molecular cues that regulate the balance between such antagonistic γδ T cell subsets in the TME remain poorly characterized. Given the strong impact of metabolic resources on anti-tumour αβ T cell responses, here we have investigated the metabolic profiles of γδ T cell subsets and how they might impact on their activities in the TME. We found that $\gamma\delta^{IFN}$ T cells are almost exclusively glycolytic, whereas $\gamma\delta^{17}$ T cells are strongly dependent on mitochondrial and lipid oxidative metabolism. This metabolic dichotomy is established in the thymus during γδ T cell development, and maintained in peripheral lymphoid organs and within tumours in various experimental models of cancer. We further show that the provision of glucose or lipids has major impact on the relative expansion and function of the two γδ T cell subsets, and this can be used to enhance anti-tumour γδ T cell responses.

Results

Intra-tumoural γδ T cell subsets display distinct metabolic profiles

The analysis of metabolic profiles of tumour-infiltrating γδ T cells (γδ TILs) presented a major challenge: the low numbers that can be retrieved from tumour lesions in mice are largely incompatible with techniques such as Seahorse metabolic flux analysis. To overcome this difficulty, we used a newly developed protocol, SCENITH™ (*Single Cell mEtabolism by profilIng Translation inHibition)*, which is a flow cytometry-based method for profiling energy metabolism with single cell resolution[23]. This method is based on metabolism-dependent translation rates and puromycin's incorporation into nascent proteins (**Supplementary Fig. 1a**). The use of specific inhibitors allows the estimation of glucose dependence, mitochondrial dependence, glycolytic capacity and fatty acid and amino acid oxidation (FaaO) capacity (**Supplementary Fig. 1b**). We employed SCENITH™ to analyze the metabolic profiles of γδ TILs isolated from tumour lesions in well-established mouse models of breast (E0771) and colon (MC38) cancer (**Fig. 1a**). In both cancer models, and at both later (**Fig. 1b,c**) and earlier time points (**Fig. 1d,e**), we observed that $\gamma\delta^{IFN}$ cells had substantially higher glycolytic capacity, whereas $\gamma\delta^{17}$ cells were strongly dependent on mitochondrial activity (**Fig. 1b-e**). These data, obtained in cancer models, prompted us to investigate the metabolic phenotypes of γδ T cell subsets in multiple tissues at steady state.

Peripheral γδ T cell subsets show different mitochondrial and metabolic phenotypes

To explore the metabolic differences between γδ T cell subsets in peripheral tissues, we analysed mitochondria, given their central role in cellular metabolism. To distinguish between $\gamma\delta^{IFN}$ and $\gamma\delta^{17}$ cells we used CD27 expression[18-21]. $CD27^-$ γδ ($\gamma\delta^{17}$) cells displayed increased mitotracker and tetramethylrhodamine methyl ester (TMRM) staining in peripheral lymph nodes (LNs) compared to $CD27^+$ γδ ($\gamma\delta^{IFN}$) cells, indicating higher mitochondrial mass (normalised to cell size) and mitochondrial membrane potential (ΔΨm),

respectively (**Fig. 2a,b**). These differences were retained upon activation and expansion *in vitro* over 9-days (**Supplementary Fig. 2**). Importantly, the distinct mitochondrial phenotypes were also validated with another mitochondrial membrane potential dye, tetramethylrhodamine ethyl ester (TMRE), and were features of $\gamma\delta^{17}$ and $\gamma\delta^{IFN}$ cells *ex vivo* from multiple locations (**Fig. 2c**). In agreement with mitochondrial enrichment in $\gamma\delta^{17}$ cells, seahorse metabolic flux analysis of peripheral $\gamma\delta$ T cells showed higher levels of basal OXPHOS in $\gamma\delta^{17}$ cells, and conversely, increased basal levels of glycolysis in $\gamma\delta^{IFN}$ cells (**Fig. 2d-f**). These data were validated in independent experiments using SCENITH^{TM} on splenic and LN $\gamma\delta$ T cell subsets (**Fig. 2g**).

To assess if this metabolic dichotomy had an underlying transcriptional basis, we measured the mRNA levels of key mitochondrial and glycolysis-associated genes in purified peripheral $\gamma\delta^{17}$ and $\gamma\delta^{IFN}$ cells. We found systematic biases in gene expression that matched the differential metabolic programmes (**Fig. 2h,i).** Of particular note is the clear-cut segregation of two master transcriptional regulators: *Nrf1*, which orchestrates mitochondrial DNA transcription[24,25], found to be enriched in $\gamma\delta^{17}$ cells (**Fig. 2h**); and *Myc*, which controls glycolysis[26,27], that was highly overexpressed in $\gamma\delta^{IFN}$ cells (**Fig. 2i**). Myc expression was further validated using a Myc-GFP reporter mouse (**Fig. 2j**). These data collectively demonstrated that $\gamma\delta$ T cell subsets possess distinct mitochondrial and metabolic features in peripheral organs at steady state.

γδ T cell subsets are metabolically programmed in the thymus

We next aimed to understand when, during their differentiation, the metabolic differences between the two effector $\gamma\delta$ T cell subsets were established. Since most $\gamma\delta$ T cells are functionally pre-programmed in the thymus, we examined $\gamma\delta$ thymocyte sub-populations. Our recent studies have identified sequential stages of thymic $\gamma\delta$ T cell progenitor development marked by CD24, CD44 and CD45RB[19]. Early CD24^{+} ($\gamma\delta^{24+}$) precursors downregulate CD24 to become a CD24^{-}CD44^{-}CD45RB^{-} ($\gamma\delta^{TN}$) population that can generate cells committed to either IL-17 or IFN-γ expression, which display respectively CD44^{hi}CD45RB^{-}

($\gamma\delta^{17}$) and $CD44^{+}CD45RB^{+}$ ($\gamma\delta^{IFN}$) phenotypes (**Supplementary Fig 3**). By using the SCENITH^{TM} method, we found that, in both the adult (**Fig. 3a**) and newborn (**Fig. 3b**) thymus, these subsets showed the same metabolic dichotomy as in the periphery (**Fig. 2g**), although this was less distinct in $\gamma\delta$ thymocytes, likely due to the dynamic subset segregation process[19].

To investigate any potential switching of metabolic programming during $\gamma\delta$ thymocyte development, we first compared early thymic $\gamma\delta$ progenitors with more mature subpopulations already committed to IL-17 or IFN-γ production. We found that $\gamma\delta^{24+}$ and $\gamma\delta^{TN}$ progenitors stained highly for TMRE, that was lost when ΔΨm was dissipated by the ionophore carbonyl cyanide-4-(trifluoromethoxy) phenylhydrazone (FCCP) (**Fig. 3c,d**). Interestingly, whereas $\gamma\delta^{17}$ cells retained a high level of TMRE staining, $\gamma\delta^{IFN}$ cells showed a marked reduction in ΔΨm suggesting a metabolic switch away from OxPhos (**Fig. 3d**). Moreover, imagestream analysis of $\gamma\delta^{17}$ cells stained with either mitotracker or TMRE revealed large and active mitochondria, in contrast with $\gamma\delta^{IFN}$ cells that displayed negligible staining for either dye (**Fig. 3e**), in line with our previous observations in peripheral subsets (**Fig. 2a-c**). Furthermore, Seahorse extracellular flux analysis showed that $\gamma\delta^{17}$ thymocytes have both higher maximal respiration potential and spare respiratory capacity than their $\gamma\delta^{IFN}$ counterparts (**Fig. 3f,g**). Thus, $\gamma\delta$ T cell subsets acquire distinct mitochondrial features during their acquisition of effector function in the thymus.

The adoption of divergent metabolic programs by thymic $\gamma\delta$ T cell subsets suggested they could thrive under distinct metabolic environments. To begin to address this, we placed WT E15 thymic lobes in 7-day foetal thymic organ cultures (E15 + 7d FTOC) with media containing either low or high amounts of glucose (**Fig. 3h**). $\gamma\delta^{17}$ cells were readily detected in lower glucose conditions but failed to develop to normal numbers when glucose concentrations were raised. By contrast, $\gamma\delta^{IFN}$ cells were relatively enriched in high glucose conditions as demonstrated by a significant decrease in the $\gamma\delta^{17}$/ $\gamma\delta^{IFN}$ cell ratio (**Fig. 3h**). We next established E15 + 7d FTOC in the presence of the glycolysis inhibitor 2-deoxy-D-glucose (2-DG), and found increased numbers of $\gamma\delta^{17}$ cells and increased $\gamma\delta^{17}$/ $\gamma\delta^{IFN}$ cell ratios (**Fig. 3i**). A similar result was observed in

E15 + 7d FTOC when cultured with Fasentin that blocks glucose uptake (**Supplementary Fig. 4**). By contrast, running E15 + 7d FTOC in the presence of metformin, which reduces the efficiency of OxPhos by inhibiting complex I of the electron transport chain, impaired $\gamma\delta^{17}$ cell generation and decreased the $\gamma\delta^{17}$/ $\gamma\delta^{IFN}$ cell ratio (**Fig. 3j**). Collectively, these results suggest that the mitochondrial characteristics adopted by $\gamma\delta^{17}$ and $\gamma\delta^{IFN}$ cells during thymic development directly impact their ability to thrive in distinct metabolic environments.

Distinct mitochondrial activities underlie effector fate of thymic γδ T cell precursors

We next aimed to investigate the association of distinct metabolic programmes with the developmental divergence of $\gamma\delta^{17}$ and $\gamma\delta^{IFN}$ cells in the thymus. Although the $\gamma\delta^{TN}$ population, i.e. the progenitor $\gamma\delta$ cell subset that immediately precedes the surface upregulation of either CD44 or CD45RB (marking commitment to the IL-17 or IFN-γ pathways, respectively[19]) was predominantly $TMRE^{hi}$, we observed a fraction of cells with reduced TMRE staining that we reasoned might be transitioning to the $TMRE^{lo}$ state shown by $\gamma\delta^{IFN}$ cells (**Fig. 3c**). We further hypothesized that the metabolic status of $\gamma\delta^{TN}$ progenitors may predict their developmental fate. To test this, we sorted $TMRE^{hi}$ and $TMRE^{lo}$ cells from the $\gamma\delta^{TN}$ subset obtained from E15 + 7d FTOC, and cultured them for 5-days on OP9-DL1 cells that are known to support appropriate development of thymocytes[28]. As predicted, virtually all cells from the $TMRE^{lo}$ cultures upregulated CD45RB and entered the IFNγ-pathway (**Fig. 4a**); however, we were surprised that almost all cells from the $TMRE^{hi}$ cultures entered the $CD44^{hi}$ IL-17-pathway (**Fig. 4a**). This strongly suggests that $\gamma\delta^{TN}$ cells have already committed to an effector fate, and that this commitment associates with distinct mitochondrial activities.

To pursue this hypothesis further, we tested $\gamma\delta^{24+}$ progenitors that immediately precede the $\gamma\delta^{TN}$ subset; again, we observed a remarkable segregation of effector fate, with the majority of $TMRE^{lo}$ $\gamma\delta^{24+}$ cells entering the IFNγ-pathway,

and the majority of TMRE^{hi} γδ^{24+} cells entering the IL-17-pathway (**Fig. 4b**). The observation that so few TMRE^{hi} γδ^{24+} cells adopt an IFNγ-secreting fate again suggests that most γδ^{24+} progenitors have already committed to subsequent effector function. Moreover, we found that differences in TMRE levels correlated with the known[18,20,21] effector biases of Vγ1^{+} (γδ^{IFN}-biased) and Vγ4^{+} (γδ^{17}-biased) progenitors (**Fig. 4c**); and validated the early TMRE-based segregation of effector fates using only Vγ4^{+} progenitors (**Supplementary Fig 5**). Furthermore, among γδ^{24-} thymocytes along the γδ^{IFN} pathway, we observed a progressive downregulation of TMRE levels from γδ^{TN} to CD44^{-}CD45RB^{+} cells and finally γδ^{IFN} cells (**Fig. 4d**).

Given that we and others[20,21] have previously shown a key role for TCR signalling in γδ^{IFN} thymocyte differentiation, we next asked if downregulation of TMRE levels associated with hallmarks of TCR signalling. Indeed, we found that low TMRE associated with high expression of CD73 (**Fig. 4e**)**,** one of the best established markers of TCR signalling in γδ T cell development[20,28,29]. Moreover, in E15 thymic lobes, TMRE staining was reduced along with CD25 downregulation, which is another hallmark of (developmentally early) TCRγδ signalling[18,20,21] (**Fig. 4f**). Furthermore, at this E15 stage, the cells with the lowest TMRE staining were Vγ5^{+} progenitors (**Fig. 4f**) that are known to engage a Skint1-associated TCR-ligand in the thymus and to uniformly commit to the IFNγ-pathway[30].

These lines of evidence suggested that γδ progenitors receiving agonist TCRγδ signals shift away from OxPhos as indicated by their reduced ΔΨm. To strengthen this point, we manipulated TCR signals using agonist GL3 mAb, which, as expected[18,19], promoted γδ^{IFN} cell development while inhibiting the γδ^{17} pathway in E17 + 6d FTOC (**Fig. 4g**). Upon specifically sorting TMRE^{hi} γδ^{24+} cells from E17 thymi and stimulating them with GL3 for 5h, we found a subpopulation that dowregulated CD24 together with TMRE levels, in a mAb dose-dependent dose manner (**Fig. 4h**). These results strongly suggest that TCR signalling leads to ΔΨm downregulation as γδ thymocytes differentiate into IFN-γ producers.

To gain further molecular resolution, we performed single-cell RNAsequencing on TMRE^{lo} and TMRE^{hi} $\gamma\delta^{24+}$ cells from E15 + 2d FTOC (**Fig. 4i-l**). Using UMAP, TMRE^{lo} cells clustered clearly away from TMRE^{hi} $\gamma\delta^{24+}$ cells (**Fig. 4j**), and the former were enriched in genes involved in the regulation of antigen receptor signalling (**Fig. 4k**). In support of the metabolic phenotypes observed *ex vivo*, genes associated with OxPhos were enriched specifically in TMRE^{hi} $\gamma\delta^{24+}$ cells while genes involved in glucose metabolism were unregulated in TMRE^{lo} $\gamma\delta^{24+}$ cells (**Fig. 4l**).

These data collectively demonstrate that metabolic status of thymic $\gamma\delta$ progenitors marks their developmental fate from a very early stage. Progenitors entering the IL-17 pathway display sustained high mitochondrial activity, whereas those in the IFN-γ pathway undergo a TCR-induced metabolic shift towards aerobic glycolysis. We next questioned how these intrinsic metabolic differences impacted the physiology of effector $\gamma\delta$ T cell subsets.

Enrichment of lipid storage and lipid metabolism in $\gamma\delta^{17}$ cells

Having shown that, in stark contrast with $\gamma\delta^{IFN}$ cells, $\gamma\delta^{17}$ cell generation was reduced under high glucose concentrations (**Fig. 3h**), and enhanced upon inhibition of glycolysis (**Fig. 3i**) or glucose uptake (**Supplementary Fig. 4**), we questioned whether other metabolic resources may be important for $\gamma\delta^{17}$ cell physiology. To address this question we took advantage of reporter mice (*Zbtb16*^{GFP}) for another marker that segregates $\gamma\delta^{17}$ and $\gamma\delta^{IFN}$ cells, the transcription factor PLZF (encoded by *Zbtb16*)[21,14,31]. We performed RNA-sequencing of lymphoid and tissue-resident $\gamma\delta$ T cells sorted into PLZF^{+} ($\gamma\delta^{17}$) and PLZF^{-} ($\gamma\delta^{IFN}$) cells (**Fig. 5a**). As expected, $\gamma\delta^{17}$ cells across tissues expressed *Il17a*, whereas *Il17f* was also expressed in tissue-resident $\gamma\delta^{17}$ cells (**Fig. 5b**). Different metabolic pathways were associated with lymphoid versus tissue resident $\gamma\delta$ T cells however, the genes common to $\gamma\delta^{17}$ cells across all tissues were related to lipid and mitochondrial metabolism, including glutamate transporter (*Slc1a1*), glucose/fatty acid metabolism (*Pdk4*), mitochondrial protein transport (*Ablim3*) and lipid metabolism (*Fabp1*, *Abdh5*, *Atp10a*). These

data highlight genes associated with lipid metabolism as a common feature of $\gamma\delta^{17}$ T cells across tissues. Consistent with this, LN $\gamma\delta^{17}$ cells had a higher neutral lipid content (as assessed by LipidTOX staining) than $\gamma\delta^{IFN}$ cells (**Fig. 5 c,d**). This differential lipid content was further increased upon activation with IL-1β+IL-23 (**Supplementary Fig. 6a**), associated with expression of IL-17A, IL-17F and RORγt (**Supplementary Fig. 6b**), and was observed across γδ T cells from multiple tissues, with the notable exception of the skin (**Fig. 5e**), where $\gamma\delta$ T cells have been shown to display specific mechanisms of tissue adaptation[32]. In particular, V$\gamma6^+$ $\gamma\delta$ T cells in the dermis are transcriptionally distinct from those in pLNs and display a highly activated but less proliferative phenotype. This tissue adaptation may alter the metabolic requirements of skin-resident γδ T cells. In addition, $\gamma\delta$ T cells may adapt to utilize specific metabolites present within the skin[33].

Imaging analysis revealed that the increased LipidTOX staining was due to the accumulation of intracellular lipid droplets in $\gamma\delta^{17}$ cells (**Fig. 5f,g**). Lipid droplets store neutral lipids including triglycerides (TAGs) and cholesterol esters[34]. We found that the two $\gamma\delta$ subsets had equivalent TAG content (**Fig. 5h**) but free cholesterol, as determined by Filipin III staining, was higher in $\gamma\delta^{17}$ cells (**Fig. 5i**). We next questioned if $\gamma\delta^{17}$ engaged in lipid uptake which could account for lipid storage. Using labelled palmitate (Bodipy-FL-C_{16}), we found that $\gamma\delta^{17}$ cells selectively took up lipids (**Fig. 5j**), which was further enhanced following activation (**Supplementary Fig. 6c**). Analysis of $\gamma\delta$ T cell cytokine production confirmed that the ability to take up palmitate was specific to IL-17 producers (**Fig. 5l,m**). Of note, V$\gamma4^+$ and V$\gamma6^+$ (V$\gamma1^-$V$\gamma4^-$) $\gamma\delta$ T cells showed a higher palmitate uptake than V$\gamma1^+$ cells (**Fig. 5n**); While V$\gamma6^+$ $\gamma\delta$ T cells primarily produce IL-17, V$\gamma4^+$, can produce either IFN-γ or IL-17[18,19]. However, palmitate uptake was specific to V$\gamma4^+$ cells that produced IL-17 (**Fig. 5o**). Furthermore, $\gamma\delta^{17}$ cells also displayed higher uptake of fluorescently labelled cholesterol ester (Bodipy CholEsteryl FL-C_{12}) (**Fig. 5k**), indicating their ability to take up multiple types of lipids including fatty acids and cholesterol.

These data demonstrate that $\gamma\delta^{17}$ cells have an exquisite capacity to take up and accumulate intracellular lipids, and display transcriptional signatures of enhanced lipid metabolism compared to $\gamma\delta^{IFN}$ cells.

High fat diet promotes $\gamma\delta^{17}$ cell expansion and their accumulation in tumours

We next tested the effect of a lipid-rich, high fat diet (HFD), on $\gamma\delta$ T cell subsets *in vivo*. Unlike standard fat diet (SFD) fed mice, which alternate between using lipids or carbohydrates for fuel during light/dark cycles respectively, feeding mice a HFD reduced their respiratory exchange ratio (RER), illustrating a systemic metabolic switch to constantly burning lipids as the main fuel source. (**Fig. 6a**). We found that both the percentage and absolute number of LN $\gamma\delta$ T cells were increased during HFD (**Fig. 6b**), which was due to a specific increase in $\gamma\delta^{17}$ (but not $\gamma\delta^{IFN}$) cells (**Fig. 6c,d**).

Tumours are another site reported to be lipid-rich. To explore the effect of the lipid-rich tumour environment on $\gamma\delta^{17}$ cells, we employed the B16F10 melanoma model. In SFD mice, we found an enrichment of $\gamma\delta^{17}$ cells within the tumour compared to draining LN (dLN) or spleen (**Fig. 6e**). These $\gamma\delta^{17}$ cells were also enriched compared to $\gamma\delta^{IFN}$ (**Fig. 6f**). Given $\gamma\delta^{17}$ were enriched in obese mice and in the tumour, we next asked if obesity combined with the tumour model would further enhance $\gamma\delta^{17}$ cells. Mice fed HFD exhibited enhanced tumour growth (**Fig. 6g**), and further increased percentages and numbers of tumour-infiltrating $\gamma\delta^{17}$ cells compared to the SFD group (**Fig. 6 h-j**). These data demonstrate that a lipid-rich environment selectively accumulates $\gamma\delta^{17}$ but not $\gamma\delta^{IFN}$ cells in the tumour.

Given the preferential uptake of cholesterol by $\gamma\delta^{17}$ cells (**Fig. 5i**), we next investigated its effect on $\gamma\delta^{17}$ cell proliferation and function. We incubated purified $\gamma\delta^{27-}$ ($\gamma\delta^{17}$) cells for 5h with cholesterol-loaded cyclodextrin (CLC), which we found to promote $\gamma\delta^{27-}$ cell proliferation when compared to control culture conditions (**Fig. 6k**). To determine its impact on tumor growth *in vivo*, we injected CLC pre-treated (or control) $\gamma\delta^{17}$ cells twice (within two days) into s.c.

E0771 tumours (as established in **Fig. 1b**), which allow local T cell delivery. Strikingly, $\gamma\delta^{17}$ cells pre-treated with CLC substantially enhanced tumour growth (**Fig. 6l-n**).

Conversely, we also tested the effect of reducing lipids *in vivo*, by injected orlistat, which inhibits lipases and thus prevents uptake of dietary fat, into B16F10 tumour-bearing mice. Mice injected with orlistat exhibited reduced body weight and tumour growth compared to vehicle-treated mice (**Supplementary Fig. 7a,b**). Importantly, these mice showed decreased numbers of tumour-infiltrating $\gamma\delta^{17}$ cells, which had lower neutral lipid content (**Supplementary Fig. 7c,d**).

Together, these data show that lipid-rich environments promote the selective expansion of $\gamma\delta^{17}$ cells that support tumour growth.

Glucose supplementation enhances anti-tumour functions of $\gamma\delta^{IFN}$ cells

We next aimed to use the knowledge gathered in this study to boost anti-tumour $\gamma\delta$ T cell responses, which are known to rely on $\gamma\delta^{IFN}$ cells[8,22]. Given our data showing that glucose promotes the development of $\gamma\delta^{IFN}$ over $\gamma\delta^{17}$ cells in the thymus (**Fig. 3h,i**), and the higher glycolytic capacity of $\gamma\delta^{IFN}$ cells in peripheral organs (**Fig. 2g**) and also within tumours (**Fig. 1b-e**), we hypothesized that glucose supplementation would enhance $\gamma\delta^{IFN}$ cell functions. Further supporting this hypothesis, we found that intra-tumoural $\gamma\delta^{IFN}$ cells preferentially took up 2-NDBG when compared to $\gamma\delta^{17}$ TILs (**Fig. 7a**).

We first tested the impact of glucose on $\gamma\delta^{17}$ and $\gamma\delta^{IFN}$ cell functions *in vitro*. We cultured purified $\gamma\delta^{27-}$ ($\gamma\delta^{17}$) or $\gamma\delta^{27+}$ ($\gamma\delta^{IFN}$) cells in standard culture conditions containing low dose glucose (5mM) or in high glucose (50mM). We found high glucose to be detrimental to $\gamma\delta^{17}$ cells (**Supplementary Fig. 8**), in stark contrast to $\gamma\delta^{IFN}$ cells. Indeed, supplementation with high glucose augmented (whereas provision of 2-DG reduced) the percentage and numbers of $\gamma\delta^{IFN}$ cells (**Fig. 7b**), with parallel effects on their proliferation (**Fig. 7c**) and on the levels of expression of both IFN-γ (**Fig. 7d**) and its master transcriptional regulator[21], T-bet (**Fig. 7e**).

To specifically address the importance of aerobic glycolysis for $\gamma\delta^{IFN}$ cells, we cultured $\gamma\delta^{IFN}$ cells with galactose (compared to glucose), since cells grown in galactose enter the pentose phosphate pathway instead of using aerobic glycolysis[35,36]. We observed a reduction in the percentage and absolute numbers of $\gamma\delta^{IFN}$ cells (**Fig. 7f**), as well as in their IFN-γ (**Fig. 7g**) and T-bet (**Fig. 7h**) expression levels, thus establishing that aerobic glycolysis is required for optimal IFN-γ production by $\gamma\delta^{IFN}$ cells.

Next we asked if the cytotoxic function of $\gamma\delta^{IFN}$ cells was also enhanced by glucose supplementation. For this, we co-cultured $\gamma\delta^{IFN}$ cells that were previously supplemented (or not) with high dose of glucose with E0771 breast cancer cells at different effector:target (E:T) ratios. "Glucose-enhanced" $\gamma\delta^{IFN}$ cells displayed substantially higher cytotoxic potency against the cancer cells, compared to the respective controls at each E:T ratio (**Fig. 7i**).

As $\gamma\delta$ T cells are actively being pursued in the clinic as an adoptive cell therapy for cancer[8], we tested whether we could use glucose supplementation to enhance the anti-tumour functions of $\gamma\delta^{IFN}$ cells *in vivo*, in an adoptive cell transfer setting. Purified $\gamma\delta^{IFN}$ cells were cultured in the presence or absence of high dose glucose for 5h, washed, and injected twice (within two days) into the tumour site. While control $\gamma\delta^{IFN}$ cells produced a small yet significant reduction in tumour size, glucose substantially augmented the anti-tumour effects of $\gamma\delta^{IFN}$ cells, essentially inhibiting tumour growth (from the time of injection) within the time window analysed (**Fig. 7j,k**). These data reveal a new, metabolism-based, means to enhance the anti-tumour functions of $\gamma\delta$ T cells that could be explored for adoptive cell immunotherapy of cancer.

Discussion

Metabolism dysregulation is viewed as an immune evasion strategy in cancer. To overcome it, and thus enable anti-tumour immune responses, it is critical to understand immune cell metabolism and its interplay with tumour cells in the TME. Although our knowledge on αβ T cell metabolism has increased significantly[1,3,37], little is known about γδ T cells. Here, we identified a metabolic dichotomy between the main effector γδ T cell subsets that play opposing roles in cancer immunity[8,22]. Whereas anti-tumoural γδ^{IFN} cells are almost exclusively glycolytic, pro-tumoural γδ^{17} cells require mitochondrial metabolism; and their activities within tumours can be promoted by glucose or lipid metabolism, respectively.

Unexpectedly, the metabolic dichotomy of γδ T cell subsets is established early during thymic development, which contrasts with the peripheral metabolic (re)programming of effector αβ T cells. Naïve αβ T cells require activation to undergo rewiring of cellular metabolism, namely transition from OxPhos to aerobic glycolysis, through which glucose is fermented into lactate rather than oxidized in mitochondria[3]. Furthermore, depending on metabolic cues in the tissue or during immune challenge, naïve T cells are pushed toward Th1, Th2, Th17 or Treg fates, dependent on intrinsic metabolic pathways engaged outside the thymus. By contrast, we show that an equivalent metabolic shift occurs in early thymic γδ progenitors as they commit to the IFN-γ pathway, seemingly as a result of strong TCRγδ signalling. Indeed, analysis of various hallmarks of TCR signalling suggest that γδ progenitors receiving agonist TCRγδ signals shifted away from OxPhos as indicated by their reduced ΔΨm. Moreover, upon TCR (GL3 mAb) stimulation, a small population of γδ progenitors downregulated CD24 together with ΔΨm (TMRE), thus associating strong TCRγδ signalling in the γδ^{IFN} developmental pathway with metabolic reprogramming. This draws a parallel with αβ T cell activation, during which early TCR signalling is required for induction of aerobic glycolysis[38]. This acts as a switch for *Myc* mRNA (and protein) expression, such that strength of TCR stimulus determines the frequency of T cells that transcribe *Myc* mRNA[36]. The common denominator of the metabolic switches in effector γδ and αβ T cells

may thus be upregulation of Myc, which is required for transcription of genes encoding glycolytic enzymes[26,27]. Indeed, our data show a striking enrichment of Myc (mRNA and protein) in $\gamma\delta^{IFN}$ cells compared to $\gamma\delta^{17}$ cells. On the other hand, the sustained dependence of $\gamma\delta^{17}$ cells on mitochondrial OxPhos is in line with that recently reported for their functional equivalents in the $\alpha\beta$ T cell compartment, Th17 cells[39]. Of note, IL-17-producing type 3 innate lymphoid cells (ILC3) were recently shown to require both glycolysis and mitochondrial-derived ROS for activation[40], but a direct comparison with type 1 ILCs is still missing.

The concept of TCR signalling playing a key role in the metabolic programming of $\gamma\delta$ T cell subsets builds upon, but provides a novel perspective to, previous models of their thymic development. Thus, the unequivocal dependence on strong TCR signals for $\gamma\delta^{IFN}$ cell differentiation[20,30] may be linked to a required metabolic shift to aerobic glycolysis. Moreover, the detrimental impact of agonist TCR signals on $\gamma\delta^{17}$ cell development may be due to metabolic conflict with their OxPhos requirements, documented by our FTOC experiments using specific inhibitors. Importantly, these distinct metabolic phenotypes are maintained in peripheral $\gamma\delta$ T cell subsets, which is consistent with and expands our previous epigenetic and transcriptional analyses[41,42].

We were particularly interested to investigate the metabolic properties of peripheral $\gamma\delta$ T cell subsets once they infiltrated tumour lesions, for which we employed three experimental models of cancer (melanoma, breast and colon). Critically, we found that the dichotomy between $\gamma\delta^{17}$ and $\gamma\delta^{IFN}$ subsets was preserved in the TME, which enabled metabolic interventions that may have therapeutic potential. In fact, while $\gamma\delta$ T cell infiltration is largely perceived to associate with favourable prognosis in cancer patients[43], recent clinical data have suggested that, in agreement with mouse experimental systems[22], human $\gamma\delta^{17}$ *versus* $\gamma\delta^{IFN}$ cell subsets have antagonistic prognostic values[8]. Thus, improvement in the therapeutic performance of $\gamma\delta$ T cells in the clinic[44] is likely to require a better understanding of the factors that control the balance between $\gamma\delta^{17}$ and $\gamma\delta^{IFN}$ cell subsets in the TME.

Here, we also identified lipids as key γδ^{17}-promoting factors, which is particularly relevant because tumours are known to be lipid-rich microenvironments[4,5,45,46]. Palmitate and cholesterol ester uptake were higher in γδ^{17} than γδ^{IFN} cells, therefore we propose that increase in intracellular lipids is due to enhanced uptake, although endogenous lipid synthesis cannot be ruled out. Our findings that γδ^{17} cell proliferation is boosted by cholesterol treatment, and that these cells expand substantially in obese mice, provide additional evidence that HFD causes a systemic increase in the γδ^{17} subset, consistent with previous findings in the skin[47] and lungs[48], and may provide a mechanistic understanding for this expansion. Obesity is a known risk factor for cancer and we previously demonstrated the link between obesity and suppression of NK cell anti-tumour function[49]. Given that γδ^{17} cells have strong pro-tumoural effects and we find this population to be expanded in tumours of obese mice, this may represent an additional mechanism linking cancer and obesity, whereby abundant lipids favor γδ^{17} over γδ^{IFN} cells to support tumour growth.

Conversely, we found γδ^{IFN} cells, from their thymic development to intra-tumoural functions, to be boosted by glucose metabolism. Naturally, the large consumption of glucose by tumour cells[7] creates a major metabolic constraint on γδ^{IFN} TILs. Glucose restriction can impair T cell cytokine production[5,6], while production of lactate by tumour cells performing aerobic glycolysis can inhibit T cell proliferation and cytotoxic functions[50]. Therefore, we do not conceive glucose supplementation as an appropriate strategy to enhance endogenous T cell (including γδ^{IFN}) responses *in vivo*. Instead, we suggest that it should be considered in protocols used to expand/differentiate γδ T cells *ex vivo* for adoptive cell therapy. Such an "*in vitro* glucose boost" may enable stronger anti-tumour activities (namely, IFN-γ production and cytotoxicity) upon T-cell transfer, as suggested by our data using CD27^{+} γδ^{IFN} cells in the breast cancer model, although evaluation of the duration and long-term impact of this "boost" requires further investigation in slower-growing tumour models.

While we did not dissect the mechanistic link between aerobic glycolysis and IFN-γ production by CD27^{+} γδ^{IFN} cells, previous studies on αβ T cells have shown that glycolysis controls (via the enzyme GAPDH) the translation of IFN-

γ mRNA[5]. Moreover, glycolysis was shown to be essential for the cytotoxic activity of NK cells, namely their degranulation and Fas ligand expression, upon engagement of NK cell receptors (NKRs)[51]. This is particularly interesting when considering the potential of a human γδ T cell product that we developed for adoptive cell therapy of cancer, Delta One T (DOT) cells[9,52,53]. These Vδ1$^+$ T cells are induced *in vitro* to express high levels of NKRs that enhance their cytotoxicity and IFN-γ production[52-54]. We therefore propose that high dose glucose should be added to the DOT protocol as to further increase their anti-tumour potential.

In sum, this study demonstrates that thymic differentiation of effector γδ T cell subsets, besides well-established epigenetic and transcriptional regulation, includes divergent metabolic programming that is sustained in the periphery and, in particular, in the TME. It further identifies distinct metabolic resources that control the intra-tumoural activities of γδ T cell subsets, with lipids favoring γδ^{17} cells and glucose boosting γδ^{IFN} cells, which provides a new metabolism-based angle for therapeutic intervention in cancer and possibly other diseases.

Methods

Ethics statement

All mouse experiments performed in this study were evaluated and approved by the institutional ethical committee (Instituto de Medicina Molecular Orbea), the national competent authority (DGAV) under the license number 019069, UK Home Office regulations and institutional guidelines under license number 70/8758 and by the Institutional Animal Care and Use Committee of Brigham and Women's Hospital and Harvard Medical School, the Trinity College Dublin ethics committee. Euthanasia was performed by CO_2 inhalation. Anesthesia was performed by isoflurane inhalation.

Mice and tumour cell lines

C57Bl/6J WT mice and Myc-GFP mice (B6;129-Myc$^{tm1Slek/}$J) were purchased from Charles River and Jackson Laboratories. PLZF-GFP (*Zbtb16*^{GFP}) mice were generated in the laboratory of D. Sant'Angelo as described previously[1]. Mice were maintained under specific pathogen-free conditions. Standard food and water were given *ad libitum*. Where indicated, mice were fed high fat diet (HFD) (research diets) for 8 weeks. Mice were used at the foetal (embryonic day 14-18), neonatal (1-5 days old) or adult (6-12 weeks old) stages.

The E0771 murine breast adenocarcinoma cells, MC38 murine colon adenocarcinoma cells and B16.F10 melanoma cells were purchased from ATCC (Manassas, VA). Cells were maintained in Dulbecco's Modified Eagle Medium (DMEM) with 10% (vol/vol) FCS (Gibco; Thermo Fisher Scientific) and 1% (vol/vol) penicillin/streptomycin (Sigma-Aldrich).

Tumour transplantation *in vivo*

Mice were injected with 1 x 10^6 E0771 tumour cells in fat pads, 1 x 10^6 MC38 tumour cells or 2 x 10^5 cells B16 tumour cells subcutaneously into the right shaved flank. Tumour growth was measured every 2-3 days using calipers and animals were sacrificed when tumours reached a diameter (D) of 15mm, became ulcerous, or 1 or 2 weeks after tumour injection. Tumour size was

calculated using the following formula: $(D1)^2 \times (D2/2)$, D1 being the smaller value of the tumour diameter. In some experiments, mice were fed with a HFD (60% calories from lard) for 10 weeks prior to tumour injection and the HFD was continued throughout the experiment.

Comprehensive Lab Animal Monitoring System

Indirect calorimetry data were recorded using a Promethion Metabolic Cage System (Sable Systems) essentially as described previously[2]. Mice were housed individually in metabolic chambers under a 12h light/dark cycle at room temperature (22°C) with free access to food and water. Mice were acclimated for 24h in metabolic cages before recording calorimetric variables. Mice were fed either a standard chow diet or a high fat (60%) diet ad libitum for 12 weeks prior to being placed in the metabolic cages and were maintained on either diet throughout the recording.

Tissue processing and cell isolation

Tumours were collected and digested with 1mg/mL collagenase Type I, 0.4 mg/mL collagenase Type IV (Worthington) and 10 µg/mL DNase I (Sigma-Aldrich) for 30 minutes at 37°C. Cell suspension was then filtered through a 100 µm nylon cell strainer (Falcon/Corning). γδ T cells were isolated by scratching thymus, spleen and lymph node on a 70µm mesh. Lungs were minced then homogenized in RPMI 1640 using a TissueLyser (Qiagen) and filtered through 70µm mesh. Adipose tissue was processed as described previously[3]. Red blood cells were lysed using RBC Lysis Buffer (Biolegend) or ammonium chloride lysis buffer (made in-house). Single-cell suspensions of foetal and neonatal thymocytes were obtained by gently homogenizing thymic lobes followed by straining through 40µm strainers (BD).

For cell-sorting, γδ T cells were pre-enriched by depletion of $CD4^+$ and $CD8^+$ T cells, dendritic cells and B cells using biotinylated anti-CD4 (RM4-5), anti-CD8 (53-6.7), anti-CD11c (N14) and anti-CD19 (6D5) antibodies with anti-biotin microbeads (Miltenyi Biotech) by QuadroMACS or γδ T cells were purified using

TCRγ/δ T Cell Isolation Kit, mouse (Miltenyi Biotec). Cells were sorted on a FACS Aria (BD Biosciences).

Cell Culture

CD27$^-$ γδ T cells were expanded *in vitro* as previously described[4]. This protocol was adapted to expand CD27$^+$ γδ T cells by using 10ng/ml IL-2, 10ng/ml IL-15 and 20ng/ml IL-7. For downstream assays, γδ T cells were purified using TCRγ/δ T Cell Isolation Kit, mouse (Miltenyi Biotec). E*x vivo* cultures were performed using RPMI 1640 (Gibco) supplemented with 10% heat-inactivated foetal bovine serum (Gibco), 1% penicillin/streptomycin, 1% L-glutamine. For cytokine stimulation, cells were cultured with 10ng/ml IL-1β and IL-23 (Miltenyi Biotec) and/or IL-12 and IL-18 (BioLegend).

For short-term skin-draining-lymphocyte cultures, single-cell suspensions of lymphocytes were isolated from skin-draining lymph nodes from adult B6 mice. Cells were resuspended in complete RPMI medium (RPMI-1640 with 10% FCS, 1% penicillin and streptomycin, and 2 mM L-glutamine). 1 x 10^6 lymphocytes in 500 µl of complete medium were incubated for 48h in 48-well plates either under control conditions or with the addition of 5-aminoimidazole-4-carboxamide (AICAR; 1.6 mM; Sigma-Aldrich). Cells were subsequently analysed by flow cytometry.

Foetal Thymic Organ Cultures (FTOC)

E15-E17 thymic lobes from B6 mice were cultured on nucleopore membrane filter discs (Whatman) in FTOC medium (RPMI-1640 with 10% FCS, 1% penicillin and streptomycin, 50 µM β-mercaptoethanol (Invitrogen), and 2 mM L-glutamine (Sigma-Aldrich)) for 6-12 days (unless otherwise indicated). In some experiments 2-deoxyglucose (2-DG; 0.6 mM), fasentin (0.6 mM), metformin (2 mM) or oligomycin (1 nM) were added to the cultures. All thymic organ cultures were subsequently analysed by flow cytometry. In some cultures, where concentration of glucose was manipulated, “basic” FTOC

medium (RPMI-1640 [-] glucose with 10% FCS, 1% penicillin and streptomycin, 50 µM β-mercaptoethanol (Invitrogen), and 2 mM L-glutamine (Sigma-Aldrich)) was used, and glucose was added at 5mM for "low-glucose" conditions or 25mM for "high-glucose" conditions.

In some experiments, anti-TCRδ antibody (GL3; 1µg/ml unless otherwise indicated) was added to the cultures. Cultures containing antibody were rested overnight in fresh FTOC medium before analysis. All thymic organ cultures were subsequently analysed by flow cytometry.

Manipulation of γδ metabolic pathways *in vitro* and *in vivo*

Spleen and lymph nodes were harvested from C57Bl/6J mice. Cell suspensions were stained with LIVE/DEAD Fixable Near-IR (Thermo Fisher Scientific), anti-CD3ε (145-2C11), anti-TCRδ (GL3), and anti-CD27 (LG.7F9) for 15 minutes at 4°C. $CD27^+$ and $CD27^-$ γδ T cells were FACS-sorted. $CD27^+$ and $CD27^-$ γδ T cells were incubated on plate-bound anti-CD3ε (145.2C11) (10 µg/mL) in the presence of IL-7 (50 µg/mL) or IL-7 (50 µg/mL), IL-1β (10 µg/mL) and IL-23 (10 µg/mL), respectively. All cytokines were purchased from Peprotech. Then, cells were cultured with 2-Deoxy-D-Glucose (2-DG; 2mM; Sigma-Aldrich), high D-glucose (50mM; Sigma-Aldrich), galactose (20mM; Sigma-Aldrich), Carbonyl cyanide 4-(trifluoromethoxy) phenylhydrazone (FCCP; 1µM; Sigma-Aldrich) and cholesterol-loaded cyclodextrin (CLC; 5 µg/mL) for 5h at 37°C for *in vitro* experiments.

For experiments *in vivo*, purified $CD27^-$ and $CD27^+$ γδ T cells were incubated (or not) for 5h with cholesterol-loaded cyclodextrin (5 µg/mL) or with high D-glucose (50mM; Sigma-Aldrich), respectively. 5×10^5 $CD27^-$ or 1×10^6 $CD27^+$ γδ T cells were injected twice directly at the tumor site (1^{st} injection 7 days after tumour inoculation and 2^{nd} injection 2 days later). Mice were analyzed 11 days after tumour cell injection.

For lipid depletion *in vivo*, mice were injected daily with 50mg/kg Orlistat i.p. on days 6-9 after tumour injection, then tumour cell infiltrate was analysed on day 10.

Killing assays for CD27$^+$ γδ T cells *in vitro*

Purified CD27$^+$ γδ T cells were supplemented (or not) with high levels of glucose (50mM; Sigma-Aldrich) for 5h at 37°C, 5% CO_2. Then, variable numbers of CD27$^+$ γδ T cells were co-cultured with 5 x 10^5 E0771 breast cancer cells in complete RPMI Medium (minus D-Glucose). The killing capacities of CD27$^+$ γδ T cells based on death of E0771 cells (Annexin V staining) was assessed by flow cytometry after 24h.

Flow cytometry

γδ T cells were analysed by flow cytometry using standard procedures. For surface staining, cells were Fc-blocked with anti-CD16/32 (clone 93; eBioscience) and incubated for 15 minutes at 4°C with antibodies and LIVE/DEAD Fixable Near-IR (Thermo Fisher Scientific) or viability dye Zombie NIR stain (BioLegend) in FACs buffer (PBS 1X, 10% FCS, 0.5M EDTA). Anti-CD3ε (145-2C11), anti-CD27 (LG.7F9), anti-CD25 (PC61), anti-CD73 (TY/11.8) and anti-Vγ2 (UC3-10A6) were purchased from eBioscience. Anti-CD45 (30-F11), anti-TCRδ (GL3), anti-CD24 (M1/69), anti-Vγ1 (2.11), anti-Vγ4 (UC3-10A6), anti-Vγ5 (536) and anti-CD45RB (C363-16A) were purchased from BioLegend and anti-CD44 (IM7) from BD Pharmingen. Cells were washed with FACS buffer. For intracellular cytokine staining, cells were stimulated with 50 μg/mL phorbol 12-myristate 13-acetate (PMA; Sigma-Aldrich) and 1 μg/mL ionomycin (Sigma-Aldrich) for 3-4 hours at 37°C, 5% CO_2 in the presence of 10 μg/mL brefeldin-A (Sigma-Aldrich) and 2 μM monensin (eBioscience). Cells were fixed and permeabilized with Foxp3 staining kit (eBioscience/Thermo Fisher Scientific), according to the manufacturer's instructions. Cells were incubated for 30 minutes at 4°C, with the following antibodies from eBioscience: anti-IFN-γ (XMG1.2), anti-IL-17 (TC11-18H10.1), Ki67 (16A8), T-bet (4B10) and RORγt (B2D). For Annexin V staining, Annexin V Kit (eBioscience) was used following manufacturer's instructions.

The following dyes were purchased from Invitrogen and stained according to manufacturer's instructions: Mitotracker™ Green FM, Tetramethylrhodamine

Methyl Ester Perchlorate (TMRM), HCS LipidTOX™ Red Neutral Lipid Stain. Palmitate uptake was measured using 1μM Bodipy FL-C_{16} (Invitrogen) incubated for 10mins at 37°C. Cholesterol ester uptake was measured using 2μM Bodipy CholEsteryl FL-C_{12} incubated for 1h at 37°C. Cholesterol content was measured using 50μg/ml Filipin III (Sigma-Aldrich) incubated for 1h at room temperature.

Flow cytometry analysis was performed with a FACS Fortessa, LSRII or Canto II (BD Biosciences) and data analysed using FlowJo software (BD Biosciences).

Metabolism profile of cells

Seahorse Metabolic Flux Analysis**:** Real-time analysis of oxygen consumption rates (OCR) and extracellular-acidification rates (ECAR) of IFN-γ- and IL-17-committed γδ T cells sorted from 5-day-old B6 pups and $CD27^{+/-}$ γδ T cells from spleen/lymph nodes expanded *in vitro* were assessed using the XFp Extracellular Flux or Seahorse XFe-96 analyzers, respectively (Seahorse Bioscience). Cells were added to a Seahorse XF96 Cell Culture Microplate (Agilent), coated with Cell-Tak (Corning) to ensure adherence, and sequential measurements of ECAR and OCR were performed in XF RPMI Seahorse medium supplemented with glucose (10mM), glutamine (2mM), and sodium pyruvate (1mM) following the addition of Oligomycin A (2μM), FCCP (2μM), rotenone (1μM) plus antimycin A (1-4μM). Basal glycolysis, glycolytic capacity, basal mitochondrial respiration and maximal mitochondrial respiration were calculated. OCR and ECAR values were normalized to cell number.

SCENITH™

Cells were plated at 20 × 10^6 cells/ml in 96-well plates. After activation of γδ T cells, cells were treated for 30 minutes at 37°C, 5% CO_2 with Control (Co), 2-Deoxy-D-Glucose (DG; 100mM; Sigma-Aldrich), Oligomycin (O; 1μM; Sigma-Aldrich) or a combination of both drugs (DGO). Puromycin (Puro, 10μg/ml; Sigma-Aldrich) is added during 15 minutes at 37°C. SCENITH™ kit

(http://www.scenith.com) containing all reagents and protocols were kindly provided by Dr. Rafael Argüello, (CIML). Cells were washed in cold PBS and stained with primary conjugated antibodies against different surface markers (as described above) for 15 minutes at 4ºC in FACS buffer (PBS 1X 5% FCS, 2mM EDTA). After washing with FACS buffer, cells were fixed and permeabilized using Cytofix/Cytoperm™ (BD) following manufacturer's instructions. Intracellular staining of puromycin using the anti-Puro monoclonal antibody (1:600, Clone R4743L-E8) was performed by incubating cells during 30min at 4ºC diluted in Permwash. Experimental duplicates were performed in all conditions.

In vivo glucose uptake

2-NBDG (300μg diluted in PBS 1X; Cayman chemical) was injected i.v. in C57Bl/6J mice; 15min later, cells from tumours were harvested.

Assessment of mitochondrial morphology

Mitochondrial membrane potential was measured using tetramethylrhodamine, ethyl ester (TMRE; 100nM; Abcam) according to manufacturer protocols. Following TMRE staining, carbonyl cyanide-4-(trifluoromethoxy) phenylhydrazone (FCCP; 25μM; Abcam) was used as a positive control for mitochondrial membrane depolarization. Total mitochondrial mass was assessed using MitoTracker Green (Invitrogen) according to manufacturer's instructions. All cells were subsequently analysed by flow cytometry.

Triglyceride Quantification

Triglycerides (TAGs) were quantified from expanded γδ T cells *in vitro* using Picoprobe Triglyceride Quantification Assay Kit, Fluorometric (Abcam) and absorbance measured using FLUOstar OPTIMA (BMG Labtech).

RNA isolation and real-time PCR

mRNA was prepared from FACS-sorted $CD27^+$ and $CD27^-$ γδ T cells from WT spleen and draining lymph nodes using High Pure RNA Isolation kit (Roche). Reverse transcription was performed with random oligonucleotides (Invitrogen). Results were normalized to actin mRNA. qPCR was performed with SYBR Premix Ex Taq master mix (Takara) on an ABI ViiA7 cycler (Applied Biosystems). The CT for the target gene was subtracted from the CT for the endogenous reference, and the relative amount was calculated as $2^{-\Delta CT}$.

Imaging

Thymocytes from B6 E15 thymic lobes cultured for 12 days were isolated and stained for surface markers and then Mitotracker Green or TMRE (as described above). All cells were subsequently analysed on an ImageStream™ Mark II imaging flow cytometer (Amnis); 30k events were saved from samples and 1k positive events from compensation single color controls. Analysis was performed using IDEAS® version 6.2.

For lipid droplet quantification, expanded γδ T cells *in vitro* were stained with LipidTOX red neutral lipid stain (Invitrogen) and Hoechst 33342 (Sigma-Aldrich). Mitotracker Green FM (Invitrogen) was used to identify mitochondria. Cells were mounted onto poly-L-lysine coated slides. Images were obtained with a Zeiss LSM 800 confocal microscope using Zen 2.3 software (Zeiss) and analyzed using ImageJ.

RNA-sequencing and data processing

Single-cell sequencing libraries were generated using the Chromium™ Single Cell 5' Library and Gel Bead Kit (10X Genomics) according to the manufacturer's instructions. Data was analysed using the R package Seurat v2.3[5,6].

UMI counts were normalized using regularized negative binomial regression with the sctransform package[7]. For downstream analysis of normalized data principal component analysis (PCA) was performed using n=50 dimensions

and PCA variability was determined using an Elbow plot. Differential gene expression analysis and GSEA was performed using the MAST and fgsea packages[6,7]. Pathways and gene lists for gene set enrichment analysis were obtained using the misgdbr package from Molecular Signatures database (MSigDB)[8,9]. Adaptively-thresholded Low Rank Approximation (ALRA) from the Seurat wrappers package was performed to correct for drop-out values for visualization of leading-edge and differentially expressed genes identified by MAST[10]. The accession codes for single-cell RNA sequencing are GSE150585 and GSE156782.

All downstream analysis was performed using R v.3.6.3 and RStudio Desktop 1.2.5001 on an Ubuntu 19.10 linux (64 bit) system using the following R packages and libraries: dplyr v.0.8.5, fgsea v.1.12.0, ggplot2 v.3.3.0, MAST v.1.12.0, sctransform v.0.2.1, Seurat v.3.1.4, SeuratWrappers v.0.1.0, uwot v.0.1.8 and viridis v.0.5.1.

Statistical analysis

Statistical analysis was performed using GraphPad Prism software using non-parametric two-tailed Mann-Whitney test or, if both groups followed a normal distribution (tested by D'Agostino and Pearson normality test), using two-tailed unpaired Student *t* test or one-way analysis of variance. All data are presented as means ± standard error of mean (SEM) or standard deviation (SD). *p < 0.05; **p < 0.01; ***p < 0.001, ****<0.0001.

1. Lynch, L. *et al.* Regulatory iNKT cells lack expression of the transcription factor PLZF and control the homeostasis of T reg cells and macrophages in adipose tissue. *Nat. Immunol.* **16**, 85–95 (2015).
2. Vu, J. P. *et al.* Long-Term Intake of a High-Protein Diet Affects Body Phenotype, Metabolism, and Plasma Hormones in Mice. *J. Nutr.* **147**, 2243–2251 (2017).
3. Kohlgruber, A. C. *et al.* γδ T cells producing interleukin-17A regulate adipose regulatory T cell homeostasis and thermogenesis. *Nat. Immunol.* **19**, (2018).
4. McKenzie, D. R. *et al.* IL-17-producing γδ T cells switch migratory patterns between resting and activated states. *Nat. Commun.* **8**, 15632 (2017).

5. Butler, A., Hoffman, P., Smibert, P., Papalexi, E. & Satija, R. Integrating single-cell transcriptomic data across different conditions, technologies, and species. *Nat. Biotechnol.* **36**, 411–420 (2018).

6. Stuart, T. *et al.* Comprehensive Integration of Single-Cell Data Resource Comprehensive Integration of Single-Cell Data. *Cell* **177**, (2019).

7. Hafemeister, C. & Satija, R. Normalization and variance stabilization of single-cell RNA-seq data using regularized negative binomial regression. *Genome Biol.* **20**, 296 (2019).

8. Subramanian, A. *et al.* Gene set enrichment analysis: A knowledge-based approach for interpreting genome-wide expression profiles. *Proc. Natl. Acad. Sci. U. S. A.* **102**, 15545–15550 (2005).

9. Liberzon, A. *et al.* Databases and ontologies Molecular signatures database (MSigDB) 3.0. *Bioinforma. Appl. NOTE* **27**, 1739–1740 (2011).

10. Linderman, G. C., Zhao, J. & Kluger, Y. Zero-preserving imputation of scRNA-seq data using low-rank approximation. *bioRxiv* 397588 (2018). doi:10.1101/397588

Acknowledgments

We are grateful for the valuable assistance of the staff of the flow cytometry, bioimaging and animal facilities at our Institutions. We thank Ana Magalhães, Julie Ribot, Karine Serre, and Natacha Sousa (iMM) for technical suggestions and administrative help. This work was supported by the European Research Council (CoG_646701 to B.S.-S.; Stg_679173 to L.L.), Wellcome Trust (092973/Z/10/Z to D.J.P.), Science Foundation Ireland (SFI) (16/FRL/3865 to L.L), NIH (NS115064, HG008155, AG062377 to M.K), R01 AI134861, Biotechnology and Biological Sciences Research Council (BBSRC) UK (BB/R017808/1 to D.J.P) and Astrazeneca (Prémio FAZ Ciência 2019 to B.S.-S. and N.L.). N.L is supported by a post-doctoral fellowship from EMBO (ALTF 752-2018); S.M. was supported by a studentship from Medical Research Council (MRC) UK; G.F. is supported by a European Commission Marie Sklodowska-Curie Individual Fellowship (ref. 752932); and A.D, S.C. L.D and H.P are supported by Irish Research Council fellowships.

Author contributions

N.L, C.M, S.M and M.R performed most of the experiments and analyzed the data. G.F. designed and performed some experiments. N.S., A.K., L.D., H.K., A.D., S.C., H.P. R.L. and C.C. provided technical assistance in some experiments. M.K. and L.A performed bioinformatic analysis and M.B provided reagents, materials and support. R.A. provided key assistance with the SCENITH^{TM} methodology. B.S.-S., D.P and L.L conceived and supervised the study. N.L, C.M., B.S.-S., D.J.P. and L.L. wrote the manuscript.

References

1 Buck, M. D., Sowell, R. T., Kaech, S. M. & Pearce, E. L. Metabolic Instruction of Immunity. *Cell* **169**, 570-586, doi:10.1016/j.cell.2017.04.004 (2017).

2 Almeida, L., Lochner, M., Berod, L. & Sparwasser, T. Metabolic pathways in T cell activation and lineage differentiation. *Semin Immunol* **28**, 514-524, doi:10.1016/j.smim.2016.10.009 (2016).

3 Geltink, R. I. K., Kyle, R. L. & Pearce, E. L. Unraveling the Complex Interplay Between T Cell Metabolism and Function. *Annu Rev Immunol* **36**, 461-488, doi:10.1146/annurev-immunol-042617-053019 (2018).

4 Cham, C. M., Driessens, G., O'Keefe, J. P. & Gajewski, T. F. Glucose deprivation inhibits multiple key gene expression events and effector functions in CD8+ T cells. *Eur J Immunol* **38**, 2438-2450, doi:10.1002/eji.200838289 (2008).

5 Chang, C. H. *et al.* Posttranscriptional control of T cell effector function by aerobic glycolysis. *Cell* **153**, 1239-1251, doi:10.1016/j.cell.2013.05.016 (2013).

6 Chang, C. H. *et al.* Metabolic Competition in the Tumor Microenvironment Is a Driver of Cancer Progression. *Cell* **162**, 1229-1241, doi:10.1016/j.cell.2015.08.016 (2015).

7 O'Sullivan, D., Sanin, D. E., Pearce, E. J. & Pearce, E. L. Metabolic interventions in the immune response to cancer. *Nat Rev Immunol* **19**, 324-335, doi:10.1038/s41577-019-0140-9 (2019).

8 Silva-Santos, B., Mensurado, S. & Coffelt, S. B. gammadelta T cells: pleiotropic immune effectors with therapeutic potential in cancer. *Nat Rev Cancer* **19**, 392-404, doi:10.1038/s41568-019-0153-5 (2019).

9 Sebestyen, Z., Prinz, I., Dechanet-Merville, J., Silva-Santos, B. & Kuball, J. Translating gammadelta (gammadelta) T cells and their receptors into cancer cell therapies. *Nat Rev Drug Discov* **19**, 169-184, doi:10.1038/s41573-019-0038-z (2020).

10 Chien, Y. H., Meyer, C. & Bonneville, M. gammadelta T cells: first line of defense and beyond. *Annu Rev Immunol* **32**, 121-155, doi:10.1146/annurev-immunol-032713-120216 (2014).

11 Hayday, A. C. Gammadelta T cells and the lymphoid stress-surveillance response. *Immunity* **31**, 184-196, doi:10.1016/j.immuni.2009.08.006 (2009).

12 Hayday, A. C. gammadelta T Cell Update: Adaptate Orchestrators of Immune Surveillance. *J Immunol* **203**, 311-320, doi:10.4049/jimmunol.1800934 (2019).

13 Ravens, S. *et al.* Human gammadelta T cells are quickly reconstituted after stem-cell transplantation and show adaptive clonal expansion in response to viral infection. *Nat Immunol* **18**, 393-401, doi:10.1038/ni.3686 (2017).

14 Kohlgruber, A. C. *et al.* gammadelta T cells producing interleukin-17A regulate adipose regulatory T cell homeostasis and thermogenesis. *Nat Immunol* **19**, 464-474, doi:10.1038/s41590-018-0094-2 (2018).

15 Ribeiro, M. *et al.* Meningeal gammadelta T cell-derived IL-17 controls synaptic plasticity and short-term memory. *Sci Immunol* **4**, doi:10.1126/sciimmunol.aay5199 (2019).

16 Papotto, P. H., Ribot, J. C. & Silva-Santos, B. IL-17(+) gammadelta T cells as kick-starters of inflammation. *Nat Immunol* **18**, 604-611, doi:10.1038/ni.3726 (2017).

17 Jensen, K. D. *et al.* Thymic selection determines gammadelta T cell effector fate: antigen-naive cells make interleukin-17 and antigen-experienced cells make interferon gamma. *Immunity* **29**, 90-100, doi:10.1016/j.immuni.2008.04.022 (2008).

18 Ribot, J. C. *et al.* CD27 is a thymic determinant of the balance between interferon-gamma- and interleukin 17-producing gammadelta T cell subsets. *Nat Immunol* **10**, 427-436, doi:10.1038/ni.1717 (2009).

19 Sumaria, N., Grandjean, C. L., Silva-Santos, B. & Pennington, D. J. Strong TCRgammadelta Signaling Prohibits Thymic Development of IL-

17A-Secreting gammadelta T Cells. *Cell Rep* **19**, 2469-2476, doi:10.1016/j.celrep.2017.05.071 (2017).

20 Munoz-Ruiz, M. *et al.* TCR signal strength controls thymic differentiation of discrete proinflammatory gammadelta T cell subsets. *Nat Immunol* **17**, 721-727, doi:10.1038/ni.3424 (2016).

21 Munoz-Ruiz, M., Sumaria, N., Pennington, D. J. & Silva-Santos, B. Thymic Determinants of gammadelta T Cell Differentiation. *Trends Immunol* **38**, 336-344, doi:10.1016/j.it.2017.01.007 (2017).

22 Silva-Santos, B., Serre, K. & Norell, H. gammadelta T cells in cancer. *Nat Rev Immunol* **15**, 683-691, doi:10.1038/nri3904 (2015).

23 Argüello, R., Combes AJ., Char, R., Gigan, JP., Baaziz, AI., Bousiquot, E., Camosseto, V., Samad, B., Tsui, J., Yan, P., Boissoneau, S., Figarella-Branger, D., Gatti, E., Tabouret, E., Krummel, MF and Pierre, P. SCENITH: A flow cytometry based method for functional profiling energy metabolism with single cell resolution. *Cell Metabolism (in Press)* (2020).

24 Gleyzer, N., Vercauteren, K. & Scarpulla, R. C. Control of mitochondrial transcription specificity factors (TFB1M and TFB2M) by nuclear respiratory factors (NRF-1 and NRF-2) and PGC-1 family coactivators. *Mol Cell Biol* **25**, 1354-1366, doi:10.1128/MCB.25.4.1354-1366.2005 (2005).

25 Scarpulla, R. C. Nuclear control of respiratory chain expression in mammalian cells. *J Bioenerg Biomembr* **29**, 109-119, doi:10.1023/a:1022681828846 (1997).

26 Dang, C. V. *et al.* The c-Myc target gene network. *Semin Cancer Biol* **16**, 253-264, doi:10.1016/j.semcancer.2006.07.014 (2006).

27 Guo, Q. M. *et al.* Identification of c-myc responsive genes using rat cDNA microarray. *Cancer Res* **60**, 5922-5928 (2000).

28 In, T. S. H. *et al.* HEB is required for the specification of fetal IL-17-producing gammadelta T cells. *Nat Commun* **8**, 2004, doi:10.1038/s41467-017-02225-5 (2017).

29 Coffey, F. *et al.* The TCR ligand-inducible expression of CD73 marks gammadelta lineage commitment and a metastable intermediate in effector specification. *J Exp Med* **211**, 329-343, doi:10.1084/jem.20131540 (2014).

30 Turchinovich, G. & Hayday, A. C. Skint-1 identifies a common molecular mechanism for the development of interferon-gamma-secreting versus interleukin-17-secreting gammadelta T cells. *Immunity* **35**, 59-68, doi:10.1016/j.immuni.2011.04.018 (2011).

31 Lu, Y., Cao, X., Zhang, X. & Kovalovsky, D. PLZF Controls the Development of Fetal-Derived IL-17+Vgamma6+ gammadelta T Cells. *J Immunol* **195**, 4273-4281, doi:10.4049/jimmunol.1500939 (2015).

32 Tan, L. *et al.* Single-Cell Transcriptomics Identifies the Adaptation of Scart1(+) Vgamma6(+) T Cells to Skin Residency as Activated Effector Cells. *Cell Rep* **27**, 3657-3671 e3654, doi:10.1016/j.celrep.2019.05.064 (2019).

33 McCully, M. L. *et al.* Skin Metabolites Define a New Paradigm in the Localization of Skin Tropic Memory T Cells. *J Immunol* **195**, 96-104, doi:10.4049/jimmunol.1402961 (2015).

34 Bartz, R. *et al.* Lipidomics reveals that adiposomes store ether lipids and mediate phospholipid traffic. *J Lipid Res* **48**, 837-847, doi:10.1194/jlr.M600413-JLR200 (2007).

35 Le Goffe, C., Vallette, G., Jarry, A., Bou-Hanna, C. & Laboisse, C. L. The in vitro manipulation of carbohydrate metabolism: a new strategy for deciphering the cellular defence mechanisms against nitric oxide attack. *Biochem J* **344 Pt 3**, 643-648, doi:10.1042/0264-6021:3440643 (1999).

36 Bustamante, E. & Pedersen, P. L. High aerobic glycolysis of rat hepatoma cells in culture: role of mitochondrial hexokinase. *Proc Natl Acad Sci U S A* **74**, 3735-3739, doi:10.1073/pnas.74.9.3735 (1977).

37 Buck, M. D., O'Sullivan, D. & Pearce, E. L. T cell metabolism drives immunity. *J Exp Med* **212**, 1345-1360, doi:10.1084/jem.20151159 (2015).

38 Menk, A. V. *et al.* Early TCR Signaling Induces Rapid Aerobic Glycolysis Enabling Distinct Acute T Cell Effector Functions. *Cell Rep* **22**, 1509-1521, doi:10.1016/j.celrep.2018.01.040 (2018).

39 Shin, B. *et al.* Mitochondrial Oxidative Phosphorylation Regulates the Fate Decision between Pathogenic Th17 and Regulatory T Cells. *Cell Rep* **30**, 1898-1909 e1894, doi:10.1016/j.celrep.2020.01.022 (2020).

40 Di Luccia, B., Gilfillan, S., Cella, M., Colonna, M. & Huang, S. C. ILC3s integrate glycolysis and mitochondrial production of reactive oxygen species to fulfill activation demands. *J Exp Med* **216**, 2231-2241, doi:10.1084/jem.20180549 (2019).

41 Schmolka, N. *et al.* Epigenetic and transcriptional signatures of stable versus plastic differentiation of proinflammatory gammadelta T cell subsets. *Nat Immunol* **14**, 1093-1100, doi:10.1038/ni.2702 (2013).

42 Schmolka, N., Wencker, M., Hayday, A. C. & Silva-Santos, B. Epigenetic and transcriptional regulation of gammadelta T cell differentiation: Programming cells for responses in time and space. *Semin Immunol* **27**, 19-25, doi:10.1016/j.smim.2015.01.001 (2015).

43 Gentles, A. J. *et al.* The prognostic landscape of genes and infiltrating immune cells across human cancers. *Nat Med* **21**, 938-945, doi:10.1038/nm.3909 (2015).

44 Legut, M., Cole, D. K. & Sewell, A. K. The promise of gammadelta T cells and the gammadelta T cell receptor for cancer immunotherapy. *Cell Mol Immunol* **12**, 656-668, doi:10.1038/cmi.2015.28 (2015).

45 Baenke, F., Peck, B., Miess, H. & Schulze, A. Hooked on fat: the role of lipid synthesis in cancer metabolism and tumour development. *Dis Model Mech* **6**, 1353-1363, doi:10.1242/dmm.011338 (2013).

46 Ma, X. *et al.* Cholesterol Induces CD8(+) T Cell Exhaustion in the Tumor Microenvironment. *Cell Metab* **30**, 143-156 e145, doi:10.1016/j.cmet.2019.04.002 (2019).

47 Nakamizo, S. *et al.* High fat diet exacerbates murine psoriatic dermatitis by increasing the number of IL-17-producing gammadelta T cells. *Sci Rep* **7**, 14076, doi:10.1038/s41598-017-14292-1 (2017).

48 Goldberg, E. L. *et al.* Ketogenic diet activates protective gammadelta T cell responses against influenza virus infection. *Sci Immunol* **4**, doi:10.1126/sciimmunol.aav2026 (2019).

49 Michelet, X. *et al.* Metabolic reprogramming of natural killer cells in obesity limits antitumor responses. *Nat Immunol* **19**, 1330-1340, doi:10.1038/s41590-018-0251-7 (2018).

50 Fischer, K. *et al.* Inhibitory effect of tumor cell-derived lactic acid on human T cells. *Blood* **109**, 3812-3819, doi:10.1182/blood-2006-07-035972 (2007).

51 Wang, Z. *et al.* Glycolysis and Oxidative Phosphorylation Play Critical Roles in Natural Killer Cell Receptor-Mediated Natural Killer Cell Functions. *Front Immunol* **11**, 202, doi:10.3389/fimmu.2020.00202 (2020).

52 Almeida, A. R. *et al.* Delta One T Cells for Immunotherapy of Chronic Lymphocytic Leukemia: Clinical-Grade Expansion/Differentiation and Preclinical Proof of Concept. *Clin Cancer Res* **22**, 5795-5804, doi:10.1158/1078-0432.CCR-16-0597 (2016).

53 Di Lorenzo, B. *et al.* Broad Cytotoxic Targeting of Acute Myeloid Leukemia by Polyclonal Delta One T Cells. *Cancer Immunol Res* **7**, 552-558, doi:10.1158/2326-6066.CIR-18-0647 (2019).

54 Correia, D. V. *et al.* Differentiation of human peripheral blood Vdelta1+ T cells expressing the natural cytotoxicity receptor NKp30 for recognition of lymphoid leukemia cells. *Blood* **118**, 992-1001, doi:10.1182/blood-2011-02-339135 (2011).

Figure Legends

Figure 1. Intra-tumoural γδ T cell subsets display distinct metabolic profiles.

(a) Experimental design: E0771 breast or MC38 colon cancer cell lines were injected in WT mice; 6 and 15 days later, tumours were extracted for metabolic analysis of γδ T cells using SCENITH^{TM}. Inhibitors for different metabolic pathways were added for 30min followed by an incubation of 15min with puromycin. Mean fluorescence intensity (MFI) of puromycin is analyzed by flow cytometry in $\gamma\delta^{17}$ and $\gamma\delta^{IFN}$ subpopulations for each condition. **(b-e)** Puromycin MFI of $\gamma\delta^{17}$ and $\gamma\delta^{IFN}$ T cells from E0771 **(b,d)** and MC38 **(c,e)** tumour-bearing mice in control conditions (Co) or after the addition of 2-deoxy-D-glucose (DG), oligomycin (O) or both inhibitors (DGO). Graph shows the percentage of glucose dependence, mitochondrial dependence, glycolytic capacity and fatty acid and amino acid oxidation (FaaO) capacity of tumour-infiltrating $\gamma\delta^{17}$ and $\gamma\delta^{IFN}$ cells isolated either 6 **(d,e)** or 15 **(b,c)** days after cancer cell line injection. Data are representative of two independent experiments (n=5 mice per group in each experiment). pi: post-injection. $\gamma\delta^{17}$ and $\gamma\delta^{IFN}$ T cells represents IL-17 and IFN-γ-producing γδ T cells, respectively. Error bars show mean ± SEM, *p < 0.05; **p < 0.01; ****<0.0001 using unpaired Student's t-test.

Figure 2: Peripheral γδ T cell subsets show different mitochondrial and metabolic phenotypes.

(a) Representative plots (left) and summary graphs (right) of the MFI of mitotracker and tetramethylrhodamine methyl ester (TMRM) in $\gamma\delta^{27-}$ ($\gamma\delta^{17}$) and $\gamma\delta^{27+}$ ($\gamma\delta^{IFN}$) T cells *ex vivo* from LNs of C57BL/6 mice (n=7; data pooled from 2 experiments). **(b)** Representative confocal images (left) of $\gamma\delta^{17}$ and $\gamma\delta^{IFN}$ T cells stained with mitotracker (green) and Hoechst 33342 (blue). Scale bar represents 5μM. Analysis of mitotracker staining relative to cell size (right) in $\gamma\delta^{17}$ and $\gamma\delta^{IFN}$ cells *ex vivo*. Relative mitotracker was calculated by dividing the MFI of mitotracker by the MFI of FSC-A and multiplying by 100 (n=7, data pooled from 2 independent experiments). **(c)** Tetramethylrhodamine ethyl ester

(TMRE) MFI of $\gamma\delta^{17}$ and $\gamma\delta^{IFN}$ T cells from skin draining LNs, mesenteric LNs, spleen and liver of WT mice. Data are representative of 3 independent experiments (n=3 mice per group and experiment). **(d)** Seahorse analysis of extracellular acidification rate (ECAR) and oxygen consumption rate (OCR) of $\gamma\delta^{17}$ and $\gamma\delta^{IFN}$ T cells (expanded *in vitro*) from LNs ($\gamma\delta^{17}$ n=2, $\gamma\delta^{IFN}$ n=5, data representative of 3 independent experiments). **(e)** Energy map showing ECAR vs OCR of $\gamma\delta^{17}$ and $\gamma\delta^{IFN}$ T cells. Each symbol represents average basal metabolism. **(f)** Basal glycolytic rate, glycolytic capacity and basal OxPhos of $\gamma\delta^{17}$ (n=3) and $\gamma\delta^{IFN}$ (n=8) cell subsets (data pooled from 2 independent experiments). **(g)** Percentage of glucose dependence, mitochondrial dependence, glycolytic capacity and fatty acid and amino acid oxidation (FaaO) capacity of $\gamma\delta^{17}$ and $\gamma\delta^{IFN}$ cells from spleen and draining lymph nodes (dLNs). Data are representative of three independent experiments (n=5 mice per group and per experiment). **(h,i)** OxPhos-related genes (*Ndufa11, Ndufa13, Sdha, Cox6a1, Cox7a1, Cox15, Nrf1*) and glycolysis-related genes (*Pgm1, Pgm2, Gpi1, Pgam1, Myc*) were measured by qPCR in purified $\gamma\delta^{17}$ (n=4) and $\gamma\delta^{IFN}$ (n=4) T cells from spleen and dLN from WT mice. **(j)** Representative plot (left) and percentages (right) of Myc-GFP+ $\gamma\delta^{17}$ and $\gamma\delta^{IFN}$ T cells from LNs of Myc-GFP reporter mice (n=2). Error bars show mean ± SEM or SD, *p < 0.05; **p < 0.01; ***p < 0.001, ****<0.0001 using unpaired Student's t-test.

Figure 3: γδ T cell subsets are metabolically programmed in the thymus.

(a) Puromycin MFI of $\gamma\delta^{17}$ ($CD44^{hi}CD45RB^{-}$) and $\gamma\delta^{IFN}$ ($CD44^{+}CD45RB^{+}$) T cells from WT adult thymus in resting conditions (Co) and after the addition of 2-deoxy-D-glucose (DG), oligomycin (O) or both (DGO). Histogram (right) shows the percentage of glucose dependency (white), mitochondrial dependency (blue), glycolytic capacity (red) and fatty acid and amino acid oxidation (FaaO) capacity (purple) of thymic $\gamma\delta^{17}$ and $\gamma\delta^{IFN}$ cells. Data are representative of two independent experiments (n=5 mice per group and per experiment). **(b)** Histograms shows the percentage of glucose dependency (white), mitochondrial dependency (blue), glycolytic capacity (red) and fatty acid and amino acid oxidation (FaaO) capacity (purple) of $\gamma\delta^{17}$ and $\gamma\delta^{IFN}$ T cells from WT

newborn thymus (d3). Data are representative of three independent experiments (n=6 mice per group and per experiment). **(c)** Flow cytometry profile and Tetramethylrhodamine ethyl ester (TMRE) MFI of thymic $\gamma\delta^{24+}$ precursors treated or not with FCCP. Data are representative of 3 independent experiments (data points represent at least 4 lobes pooled per group and per experiment). **(d)** Flow cytometry profiles and TMRE MFI of thymic $\gamma\delta^{TN}$ ($CD44^{-}$ $CD45RB^{-}$), $\gamma\delta^{17}$ ($CD44^{hi}CD45RB^{-}$) and $\gamma\delta^{IFN}$ ($CD44^{+}CD45RB^{+}$) cells treated or not with FCCP. Data are representative of 3 independent experiments (data points represent at least 4 lobes pooled per group and per experiment). **(e)** Imagestream analysis of $\gamma\delta^{17}$ and $\gamma\delta^{IFN}$ cells stained with either mitotracker green or TMRE. Data are representative of 2 independent experiments. **(f)** O_2 consumption rates (OCR) of $\gamma\delta^{17}$ and $\gamma\delta^{IFN}$ cells were measured by Seahorse analysis in real-time under basal conditions and in response to indicated mitochondrial inhibitors. **(g)** Histograms show maximal respiration potential and spare respiratory capacity by measuring oxygen consumption rates (OCR) of $\gamma\delta^{17}$ and $\gamma\delta^{IFN}$ cells from thymuses of 5-day old B6 pups. Data are representative of 3 independent experiments (pooled thymic lobes from n>10 mice per group per experiment). **(h-j)** Flow cytometry profiles of thymic $\gamma\delta^{TN}$, $\gamma\delta^{17}$ and $\gamma\delta^{IFN}$ cells from 7-day FTOC of E15 thymic lobes either with media containing low (5mM) or high (25mM) glucose **(h)**, or with or without 2-deoxy-d-glucose (2-DG) **(i)** or metformin **(j)**. Histograms show the number of $\gamma\delta^{17}$ cells and $\gamma\delta^{17}/\gamma\delta^{IFN}$ cell ratio. Data are representative of 2 **(h)** or 3 **(i-j)** independent experiments (at least 4 lobes pooled per group per experiment). Error bars show mean ± SEM or SD, *$p < 0.05$, **$p < 0.01$, ***$p < 0.001$, ****$p < 0.0001$ using unpaired Student's t-test.

Figure 4: Distinct mitochondrial activities underlie effector fate of thymic γδ T cell progenitors.

(a,b) Flow cytometry profiles and percentage of thymic $\gamma\delta^{17}$ and $\gamma\delta^{IFN}$ cell output from post-sorted $TMRE^{lo}$ and $TMRE^{hi}$ $\gamma\delta^{TN}$ cells **(a)** or $\gamma\delta^{24+}$ cells **(b)** after 5-day culture on OP9DL1 cells. Data are representative of 3 independent experiments (n = 4 mice pooled per group per experiment). **(c)** Percentage of $V\gamma1^{+}$ and $V\gamma4^{+}$

cells in TMRE^{lo} and TMRE^{hi} $\gamma\delta^{24+}$ and $\gamma\delta^{24-}$ subsets. Data are representative of 3 independent experiments (cells sorted from n=4 mice pooled per group per experiment). **(d)** TMRE MFI of thymic $\gamma\delta^{TN}$ (CD44$^-$CD45RB$^-$), CD24$^-$CD44$^-$CD45RB$^+$ $\gamma\delta$ T cells and $\gamma\delta^{IFN}$ cells (CD44$^+$CD45RB$^+$) from 6-day FTOC of E17 B6 thymic lobes. **(e)** TMRE staining in CD24$^-$CD73$^+$, CD24$^-$CD73$^-$, CD24$^+$CD73$^+$ and CD24$^+$CD73$^-$ $\gamma\delta$ T cells from 7-day FTOC of E15 B6 thymic lobes. **(f)** TMRE staining in CD25$^-$CD24$^+$ ($\gamma\delta^{24+}$ cells), CD25^{med}, CD25^{hi} and Vγ5$^+$ $\gamma\delta$ progenitors from E15 thymus. **(g)** Flow cytometry profiles of thymic $\gamma\delta^{TN}$, $\gamma\delta^{17}$ and $\gamma\delta^{IFN}$ cells from 6-day FTOC of E17 B6 thymic lobes stimulated or not with anti-TCRδ mAb (GL3; 1µg/ml). Graph shows percentage of $\gamma\delta^{17}$ and $\gamma\delta^{IFN}$ cells in each condition. **(h)** FACS-sorted $\gamma\delta^{24+}$TMRE^{hi} cells from E17 thymi were cultured (or not) for 5h with different concentrations (as indicated) of anti-TCRδ mAb (GL3). TMRE levels were analysed by flow cytometry in $\gamma\delta^{24-}$ and $\gamma\delta^{24+}$ cells. Data are representative of 3 independent experiments (n=4 mice pooled per group per experiment). **(i)** Experimental design for single-cell RNAseq (10x Genomics) on TMRE^{lo} and TMRE^{hi} $\gamma\delta^{24+}$ cells from E15 + 2d FTOC. **(j)** Clustering of single TMRE^{lo} and TMRE^{hi} $\gamma\delta^{24+}$ cells using UMAP. **(k)** GO term analysis of genes upregulated in TMRE^{lo} versus TMRE^{hi} $\gamma\delta^{24+}$ cells. **(l)** Heatmap of differentially upregulated genes from comparison of TMRE^{lo} and TMRE^{hi} $\gamma\delta^{24+}$ cells. Genes are grouped in relation to their function in either OxPhos or glucose metabolism. Error bars show mean ± SD, *$p < 0.05$, **$p < 0.01$, ***$p < 0.001$, ****$p < 0.0001$ using unpaired Student's t-test.

Figure 5. $\gamma\delta^{17}$ cells show higher lipid uptake and lipid droplet content than $\gamma\delta^{IFN}$ cells.

(a) Experimental set up for bulk RNA-sequencing of PLZF$^+$ ($\gamma\delta^{17)}$ and PLZF$^-$ ($\gamma\delta^{IFN}$) cells isolated from PLZF-GFP (*Zbtb16*^{GFP}) mice. **(b)** Quadrant plot of genes upregulated in tissue resident PLZF$^+$ $\gamma\delta$ T cells (lower right), lymphoid PLZF$^+$ $\gamma\delta$ T cells (upper left), PLZF$^+$ $\gamma\delta$ T cells from all tissues (upper right) or PLZF$^-$ $\gamma\delta$ T cells from all tissues (lower left). **(c)** Representative histogram of neutral lipid staining (LipidTOX) in *ex vivo* $\gamma\delta^{17}$ (CD27$^-$) and $\gamma\delta^{IFN}$ (CD27$^+$) cells

from LNs. **(d)** LipidTOX MFI in $\gamma\delta^{17}$ and $\gamma\delta^{IFN}$ cells *ex vivo* from LNs as shown in (a) (n=11, data pooled from 3 independent experiments). **(e)** LipidTOX MFI in $\gamma\delta^{17}$ and $\gamma\delta^{IFN}$ cells from spleen, LNs, lungs, adipose, liver and skin (n=5-8, data pooled from 2 independent experiments). **(f)** Confocal imaging of $\gamma\delta^{17}$ and $\gamma\delta^{IFN}$ cells expanded *in vitro* and stained with LipidTOX (red) and Hoechst 33342 (blue). Scale bar represents 5μM (data representative of a minimum 10 images from 2 independent experiments). **(g)** Quantification of confocal imaging as shown in (d) (each data point represents the average per cell per image). **(h)** Quantification of triglyceride (TAG) levels from $\gamma\delta^{17}$ and $\gamma\delta^{IFN}$ cells expanded *in vitro* (n=7, each symbol represents one biological replicate). **(i)** Filipin III staining of $\gamma\delta^{17}$ and $\gamma\delta^{IFN}$ cells *ex vivo* from LNs. Representative histogram (left) and MFI (right) (n=6, data pooled from 2 independent experiments). **(j)** Representative histogram of Bodipy-FL-C_{16} uptake in $\gamma\delta^{17}$ and $\gamma\delta^{IFN}$ cells from LNs *ex vivo* (n=8, data pooled from 2 independent experiment). **(k)** Representative plots of Bodipy-FL-C_{16} uptake and IL-17 or IFN-γ production by $\gamma\delta^{17}$ and $\gamma\delta^{IFN}$ cells from LNs stimulated with PMA/ionomycin. **(l)** Bodipy-FL-C_{16} MFI in IFN-γ^+ and IL-17^+ γδ T cells (n=4, data representative of 3 independent experiments). **(m)** Representative plot of Vγ1 and Vγ4 expression in total γδ T cells and percentage Bodipy-FL-C_{16} uptake by LN γδ T cell subsets (V$\gamma1^+$, V$\gamma4^+$, V$\gamma1^-4^-$) (n=6, data pooled from 2 independent experiment). **(n)** Representative IFN-γ and IL-17 production by V$\gamma4^+$ γδ T cells from LNs and percentage Bodipy-FL-C_{16} uptake by V$\gamma4^+$IFN-γ^+ and V$\gamma4^+$IL-17^+ γδ cells (n=6, data pooled from 2 independent experiments). **(o)** Percentage Bodipy CholEsteryl FL-C_{12} uptake by $\gamma\delta^{17}$ (CD27^-) and $\gamma\delta^{IFN}$ (CD27^+) cells from LNs *ex vivo* (n=6, data pooled from 2 independent experiments). Error bars show mean ± SD, *p < 0.05, **p < 0.01, ***p < 0.001, ****p < 0.0001 using unpaired Student's t-test.

Figure 6. High fat diet promotes the expansion of $\gamma\delta^{17}$ cells in lymph nodes and within tumours.

(a) Respiratory exchange ratio (RER) of mice fed SFD or HFD for 8 weeks (n=3, data from 1 experiment). **(b)** Bar graphs showing the percentage and absolute numbers of $CD3^+$ $\gamma\delta$ T cells from LNs of standard fat diet (SFD) and high fat diet (HFD) mice (n=9, data pooled from 3 independent experiments). **(c)** Proportion of $\gamma\delta^{17}$ ($CD27^-$) and $\gamma\delta^{IFN}$ ($CD27^+$) T cells in LNs of SFD and HFD fed mice (n=9, data pooled from 3 independent experiments). **(d)** Percentage and absolute numbers of $CD27^+$ IFN-γ^+ and $CD27^-$ IL-17^+ $\gamma\delta$ T cells from LNs of SFD and HFD mice (n=9, data pooled from 3 independent experiments). **(e)** Proportion of infiltrating $\gamma\delta^{17}$ cells in spleen, draining LN and tumour in the B16 tumour model (dLN and tumour n=30, data pooled from 4 independent experiments, spleen n=7, naïve LN n=5). **(f)** Bar graph showing the percentage of $\gamma\delta^{17}$ and $\gamma\delta^{IFN}$ cells infiltrating tumours (n=9, data pooled from 2 experiments). **(g)** Bar graph represents the size of tumours (mm^3) in SFD and HFD fed mice. **(h)** Bar graph showing proportion of infiltrating $\gamma\delta^{17}$ ($CD27^-$) and $\gamma\delta^{IFN}$ ($CD27^+$) cells in tumours of SFD and HFD fed mice (SFD n=10, HFD n=12, data pooled from 2 independent experiments). **(i)** Representative plots of IL-17 and IFN-γ expression in $\gamma\delta$ T cells infiltrating tumours of SFD and HFD fed mice. Bar graphs represent the percentage of $\gamma\delta^{17}$ and $\gamma\delta^{IFN}$ cells infiltrating tumours (SFD n=17, HFD n=20, data pooled from 3 independent experiments). **(j)** Bar graph showing the number/mm^3 of $\gamma\delta^{17}$ and $\gamma\delta^{IFN}$ cells in tumours of mice on SFD or HFD **(**SFD n=7, HFD n=8, data pooled from 2 independent experiments). **(k)** Plots of proliferating $Ki67^+$ $\gamma\delta^{17}$ cells cultured for 5h with or without cholesterol-loaded cyclodextrin (CLC). Graph represents the percentage of $Ki67^+$ $\gamma\delta^{17}$ cells (data are representative of two independent experiments; pool of 3-5 mice per experiment). **(l)** $\gamma\delta^{17}$ cells cultured (or not) with cholesterol-loaded cyclodextrin (CLC) for 5h were injected s.c. into E0771 tumours at d7 and d9 after tumour cell injection. Representative picture of tumours observed at day 11 post-E0771 cell inoculation. **(m)** Graph showing tumour weight at day 11 post-E0771 inoculation. **(n)** E0771 tumour growth was monitored every two days after inoculation ((l-n) data are representative of three independent experiments

(pool of 2-5 mice per experiment). Error bars show mean ± SD, *p < 0.05, **p < 0.01, ***p < 0.001, ****p < 0.0001 using unpaired Student's t-test or ANOVA test.

Figure 7: Glucose supplementation enhances the effector functions of $\gamma\delta^{IFN}$ cells.

(a) Glucose uptake assessed upon i.v. injection of fluorescent 2-NBDG in tumour-bearing mice. Tumours were harvested 15 min later for analysis. Histogram represents 2-NBDG uptake in $\gamma\delta^{17}$ and $\gamma\delta^{IFN}$ cells. **(b-i)** Purified splenic and peripheral lymph nodes $\gamma\delta^{IFN}$ T cells ($CD3^+TCR\gamma\delta^+CD27^+$) were cultured in the presence of IL-7 with media containing low glucose (5mM), 2-deoxyglycose (2-DG), high glucose (50mM) or galactose (20mM) for 78h. **(b)** Plots of peripheral $\gamma\delta^{IFN}$ T cells cultured with IL-7 and media containing low glucose, 2-DG or high glucose. Histogram represents the fold change in number of $\gamma\delta^{IFN}$ T cells cultured with 2-DG or high glucose versus low glucose. **(c)** Fold change in number of proliferating Ki-67^+ $\gamma\delta^{IFN}$ cells cultured with 2-DG or high glucose versus low glucose. **(d,e)** IFN-γ **(d)** and T-bet **(e)** expression was analysed by flow cytometry in $\gamma\delta^{IFN}$ cells incubated with media containing low glucose, 2-DG or high glucose. Histograms show the MFI of IFN-γ and T-bet. **(f)** Flow cytometry profiles of peripheral $\gamma\delta^{IFN}$ T cells cultured with IL-7 and media containing glucose (50mM) or galactose (20mM). Histogram represents the numbers of $\gamma\delta^{IFN}$ T cells. **(g,h)** IFN-γ **(g)** and T-bet **(h)** expression was analysed by flow cytometry in $\gamma\delta^{IFN}$ cells incubated with media containing glucose or galactose. Histograms show the MFI of IFN-γ and T-bet. **(i)** Representative histograms and summary of killing assay *in vitro* of E0771 tumour cells by $\gamma\delta^{IFN}$ T cells previously supplemented (or not) with glucose (5h pre-incubation). **(j)** Representative picture of tumours observed at day 11 post-E0771 inoculation. $\gamma\delta^{IFN}$ cells supplemented (or not) with glucose for 5h were injected into the tumour at d7 and d9 after tumour cell injection. **(k)** The E0771 tumour growth was monitored every two days during 11 days after E0771 inoculation (data are representative of two **(i-k)** or four **(b-h)** independent experiments; n = 5-10 mice per group and per experiment). Error

bars show mean ± SEM, *p < 0.05, **p < 0.01, ***p < 0.001, ****p < 0.0001 using unpaired Student’s t-test or ANOVA test.

Figure 1

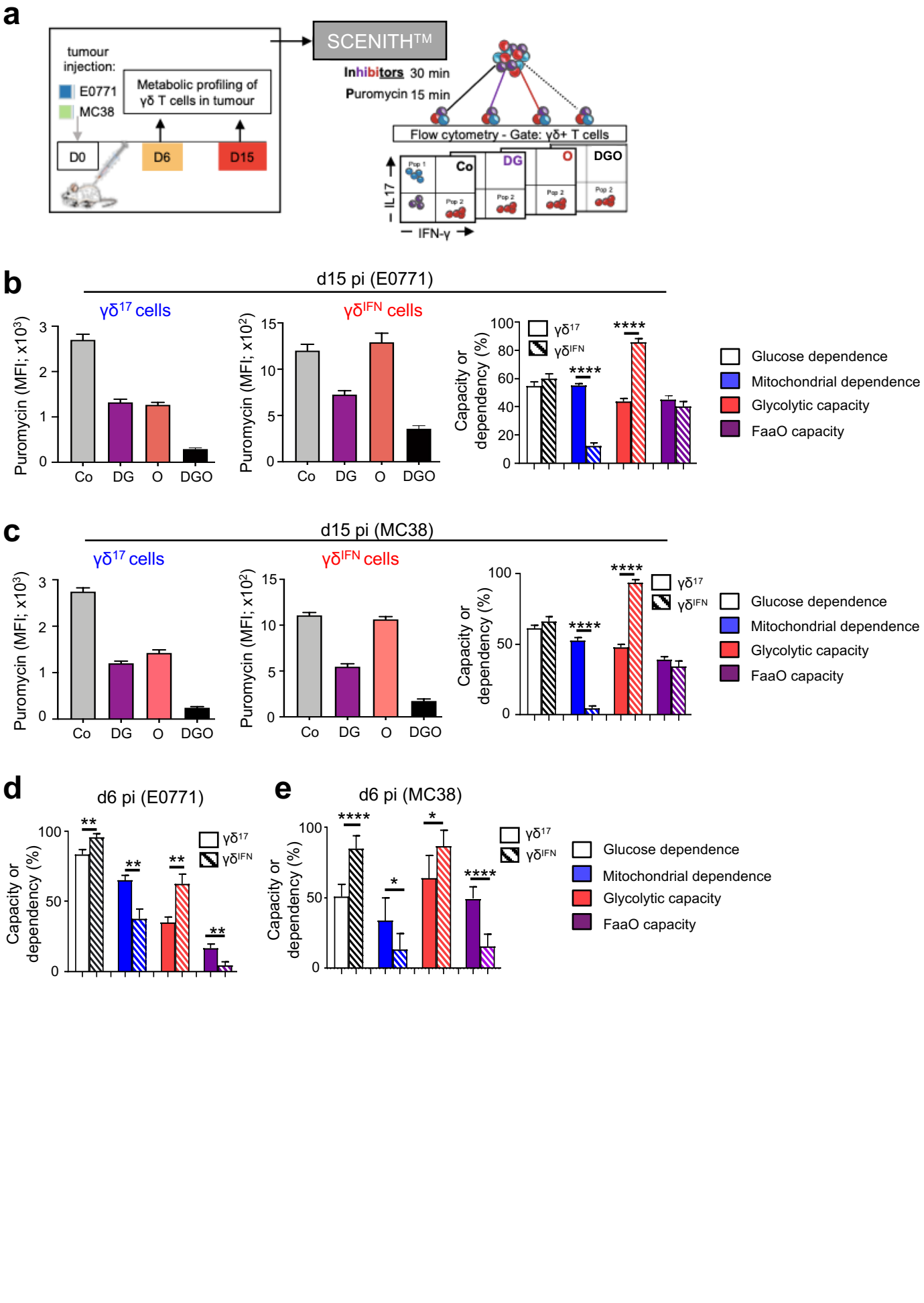
a
tumour injection:
E0771
MC38
Metabolic profiling of γδ T cells in tumour
D0
D6
D15
SCENITH™
Inhibitors 30 min
Puromycin 15 min
Flow cytometry - Gate: γδ+ T cells
Co
DG
O
DGO
IL17
IFN-γ
b
d15 pi (E0771)
γδ17 cells
γδIFN cells
Puromycin (MFI; x10³)
Puromycin (MFI; x10²)
Capacity or dependency (%)
Co DG O DGO
γδ17
γδIFN
Glucose dependence
Mitochondrial dependence
Glycolytic capacity
FaaO capacity
c
d15 pi (MC38)
d
d6 pi (E0771)
e
d6 pi (MC38)

Figure 2

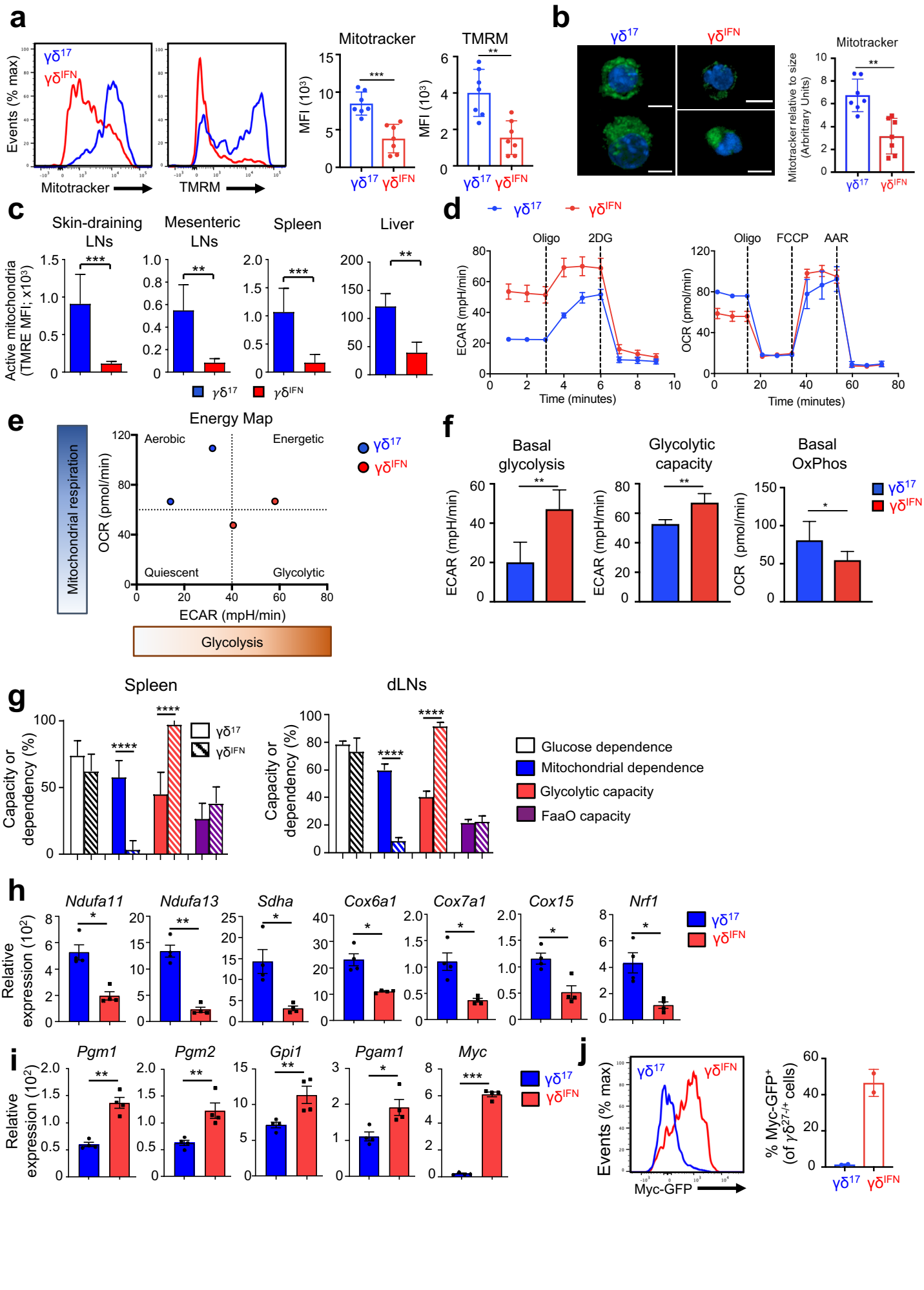
a
Events (% max)
γδ17
γδIFN
Mitotracker
TMRM
Mitotracker
TMRM
MFI (10³)
b
γδ17
γδIFN
Mitotracker
Mitotracker relative to size (Arbitrary Units)
c
Skin-draining LNs
Mesenteric LNs
Spleen
Liver
Active mitochondria (TMRE MFI; x10³)
d
Oligo
2DG
FCCP
AAR
ECAR (mpH/min)
OCR (pmol/min)
Time (minutes)
e
Energy Map
Aerobic
Energetic
Quiescent
Glycolytic
Mitochondrial respiration
OCR (pmol/min)
ECAR (mpH/min)
Glycolysis
f
Basal glycolysis
Glycolytic capacity
Basal OxPhos
g
Spleen
dLNs
Capacity or dependency (%)
Glucose dependence
Mitochondrial dependence
Glycolytic capacity
FaaO capacity
h
Ndufa11
Ndufa13
Sdha
Cox6a1
Cox7a1
Cox15
Nrf1
Relative expression (10²)
i
Pgm1
Pgm2
Gpi1
Pgam1
Myc
j
Events (% max)
Myc-GFP
% Myc-GFP⁺ (of γδ27-/+ cells)

Figure 3

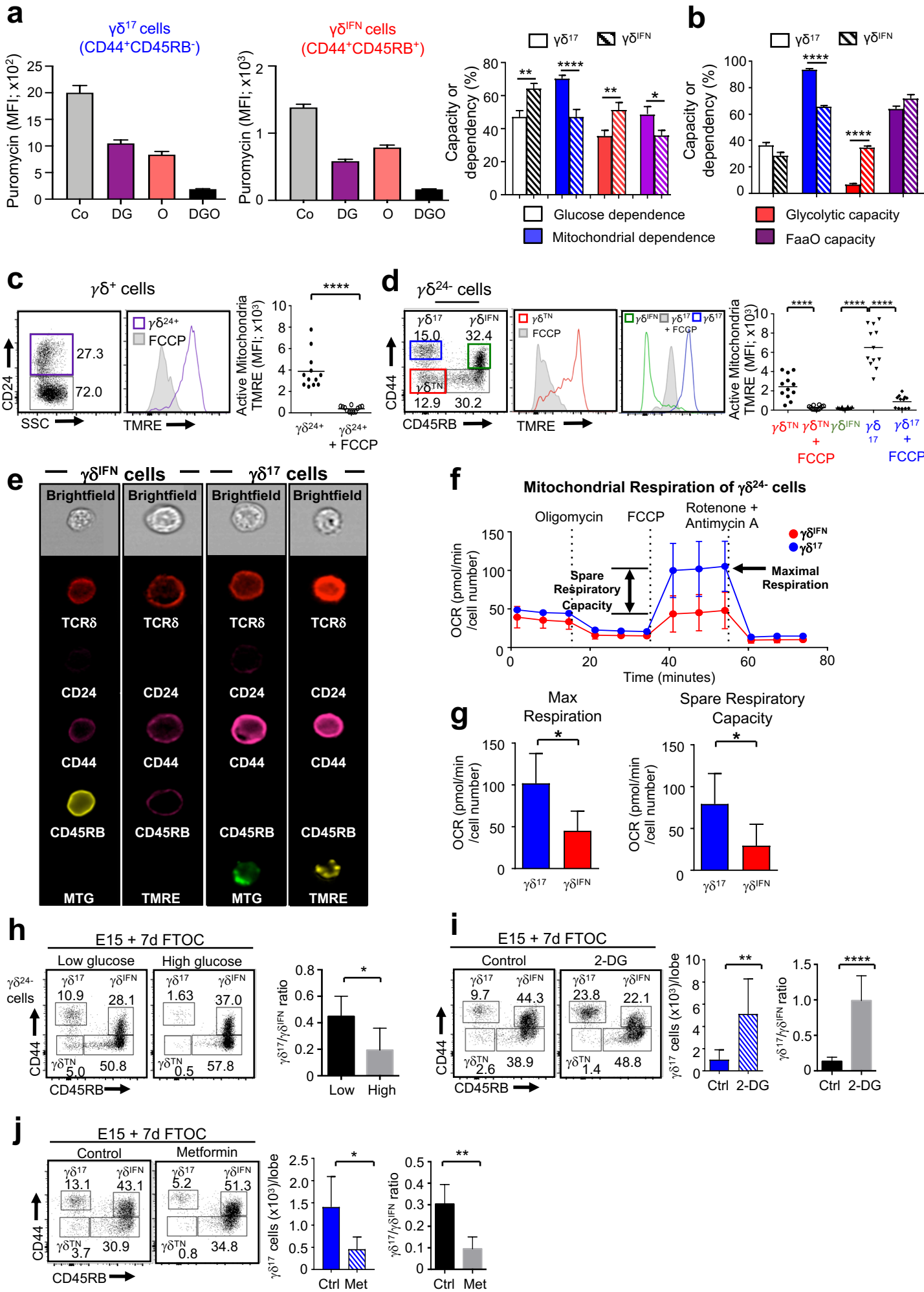
a
γδ17 cells (CD44+CD45RB-)
γδIFN cells (CD44+CD45RB+)
Puromycin (MFI; x10²)
Puromycin (MFI; x10³)
Co
DG
O
DGO
Capacity or dependency (%)
γδ17
γδIFN
Glucose dependence
Mitochondrial dependence
b
Glycolytic capacity
FaaO capacity
c
γδ+ cells
CD24
SSC
27.3
72.0
γδ24+
FCCP
TMRE
Active Mitochondria TMRE (MFI; x10³)
γδ24+ + FCCP
d
γδ24- cells
CD44
CD45RB
15.0
32.4
12.9
30.2
γδTN
+ FCCP
e
γδIFN cells
γδ17 cells
Brightfield
TCRδ
CD24
CD44
CD45RB
MTG
TMRE
f
Mitochondrial Respiration of γδ24- cells
Oligomycin
FCCP
Rotenone + Antimycin A
OCR (pmol/min /cell number)
Spare Respiratory Capacity
Maximal Respiration
Time (minutes)
g
Max Respiration
Spare Respiratory Capacity
h
E15 + 7d FTOC
Low glucose
High glucose
γδ24- cells
10.9
28.1
1.63
37.0
5.0
50.8
0.5
57.8
γδ17/γδIFN ratio
Low
High
i
Control
2-DG
9.7
44.3
23.8
22.1
2.6
38.9
1.4
48.8
γδ17 cells (x10³)/lobe
Ctrl
2-DG
j
Metformin
13.1
43.1
5.2
51.3
3.7
30.9
0.8
34.8
Met

Figure 4

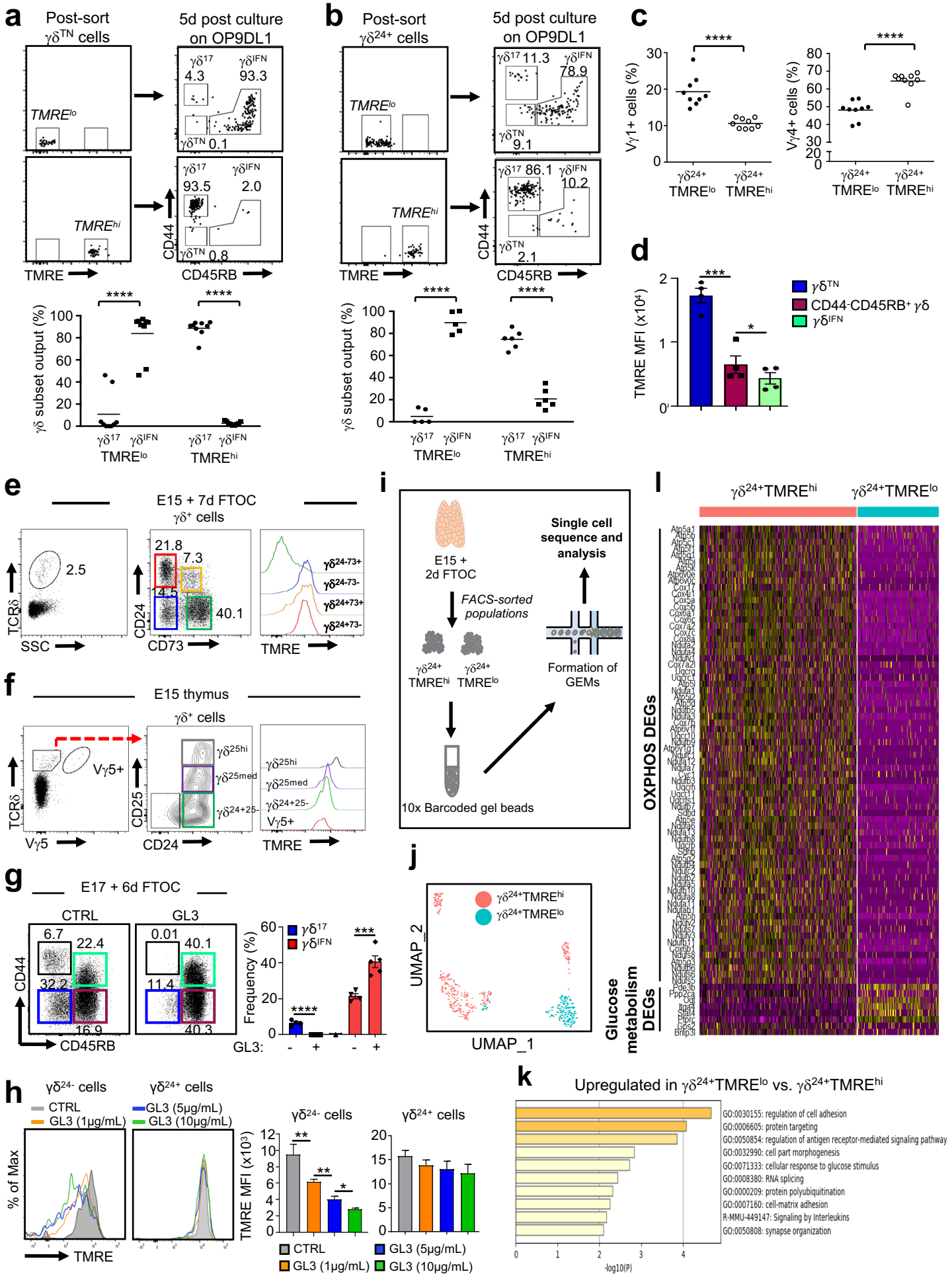
a
Post-sort γδTN cells
5d post culture on OP9DL1
TMRElo
TMREhi
γδ17 4.3
γδIFN 93.3
γδTN 0.1
γδ17 93.5
γδIFN 2.0
γδTN 0.8
CD44
TMRE
CD45RB
γδ subset output (%)
γδ17 γδIFN
TMRElo TMREhi
b
Post-sort γδ24+ cells
5d post culture on OP9DL1
γδ17 11.3
γδIFN 78.9
γδTN 9.1
γδ17 86.1
γδIFN 10.2
γδTN 2.1
c
Vγ1+ cells (%)
Vγ4+ cells (%)
γδ24+ TMRElo
γδ24+ TMREhi
d
TMRE MFI (x10⁴)
γδTN
CD44-CD45RB+ γδ
γδIFN
e
E15 + 7d FTOC
γδ+ cells
TCRδ
SSC
CD24
CD73
γδ24-73+
γδ24-73-
γδ24+73+
γδ24+73-
f
E15 thymus
γδ+ cells
Vγ5+
Vγ5
CD25
γδ25hi
γδ25med
γδ24+25-
g
E17 + 6d FTOC
CTRL
GL3
CD44
CD45RB
Frequency (%)
GL3:
h
γδ24- cells
γδ24+ cells
CTRL
GL3 (1μg/mL)
GL3 (5μg/mL)
GL3 (10μg/mL)
% of Max
TMRE
TMRE MFI (x10³)
i
E15 + 2d FTOC
FACS-sorted populations
Single cell sequence and analysis
Formation of GEMs
10x Barcoded gel beads
j
UMAP_2
UMAP_1
l
OXPHOS DEGs
Glucose metabolism DEGs
k
Upregulated in γδ24+TMRElo vs. γδ24+TMREhi
GO:0030155: regulation of cell adhesion
GO:0006605: protein targeting
GO:0050854: regulation of antigen receptor-mediated signaling pathway
GO:0032990: cell part morphogenesis
GO:0071333: cellular response to glucose stimulus
GO:0008380: RNA splicing
GO:0000209: protein polyubiquitination
GO:0007160: cell-matrix adhesion
R-MMU-449147: Signaling by Interleukins
GO:0050808: synapse organization
-log10(P)

Figure 5

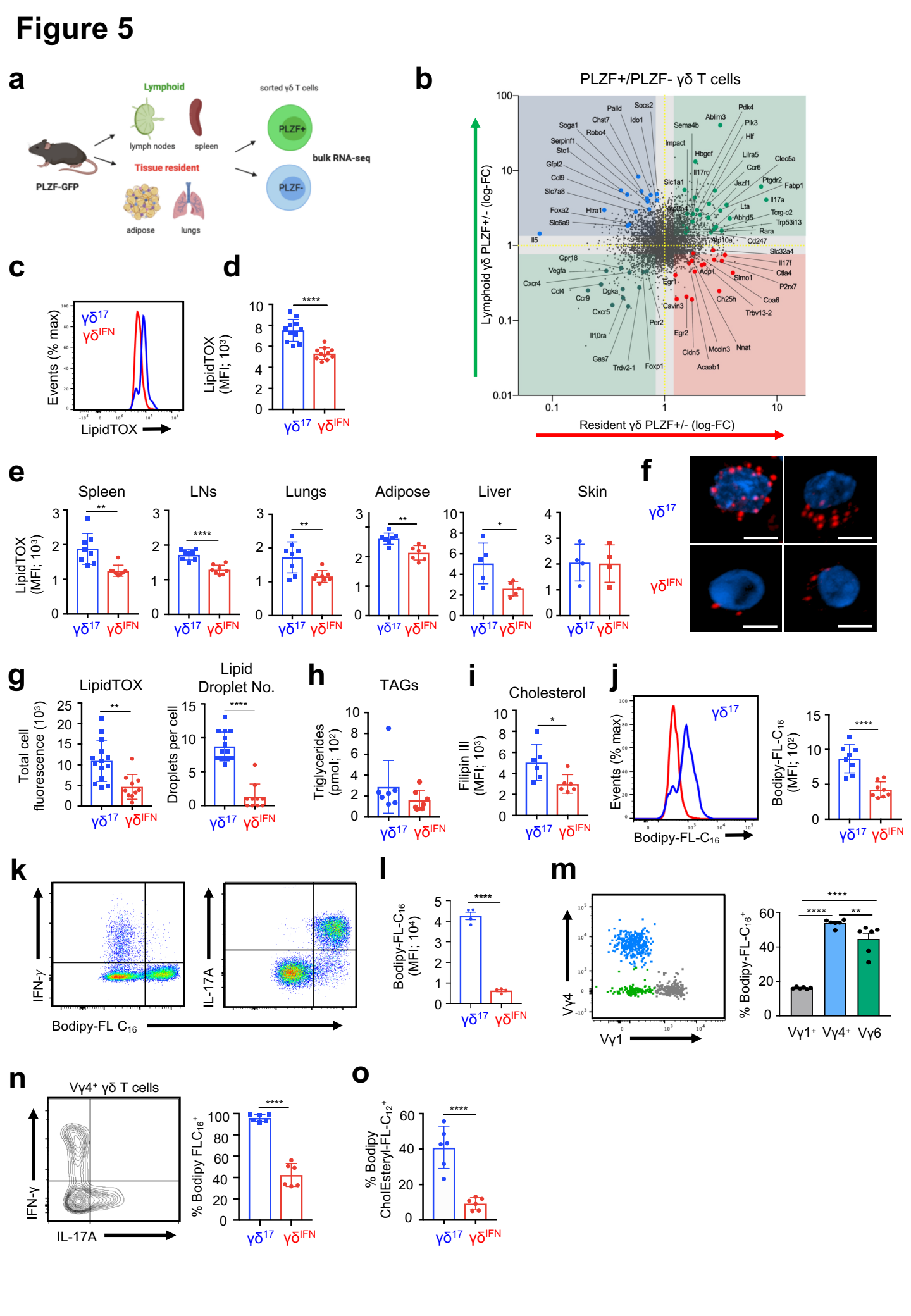
a
Lymphoid
lymph nodes
spleen
Tissue resident
adipose
lungs
PLZF-GFP
sorted γδ T cells
PLZF+
PLZF-
bulk RNA-seq
b
PLZF+/PLZF- γδ T cells
Lymphoid γδ PLZF+/- (log-FC)
Resident γδ PLZF+/- (log-FC)
c
Events (% max)
γδ17
γδIFN
LipidTOX
d
LipidTOX (MFI; 10³)
e
Spleen
LNs
Lungs
Adipose
Liver
Skin
f
g
LipidTOX
Lipid Droplet No.
Total cell fluorescence (10³)
Droplets per cell
h
TAGs
Triglycerides (pmol; 10²)
i
Cholesterol
Filipin III (MFI; 10³)
j
Bodipy-FL-C16
k
IFN-γ
IL-17A
Bodipy-FL C16
l
m
Vγ4
Vγ1
% Bodipy-FL-C16+
Vγ1+ Vγ4+ Vγ6
n
Vγ4+ γδ T cells
% Bodipy FLC16+
o
% Bodipy CholEsteryl-FL-C12+

Figure 6

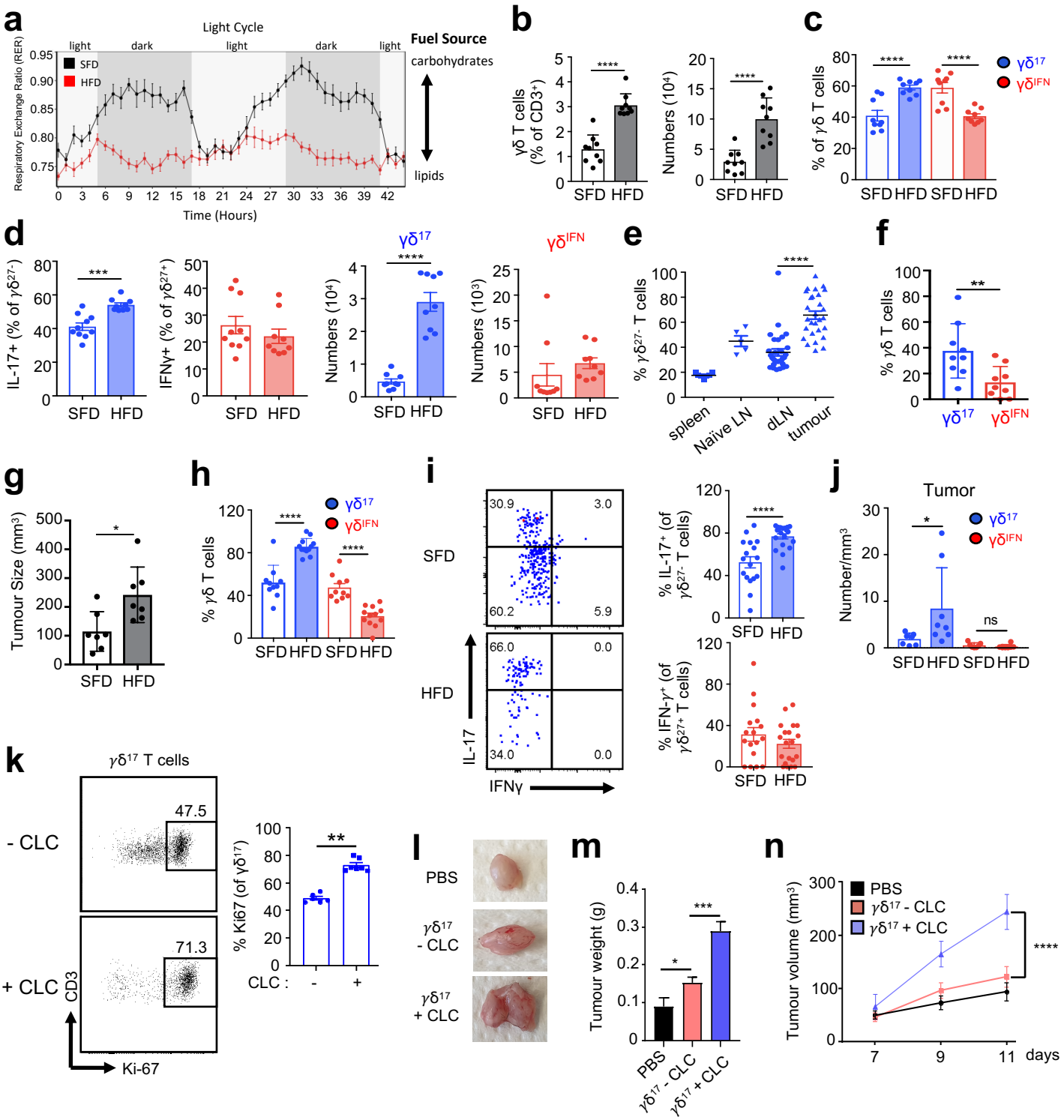
a
Light Cycle
light
dark
light
dark
light
SFD
HFD
Respiratory Exchange Ratio (RER)
Time (Hours)
Fuel Source
carbohydrates
lipids
b
γδ T cells (% of CD3+)
Numbers (10⁴)
SFD HFD
c
% of γδ T cells
γδ17
γδIFN
d
IL-17+ (% of γδ27-)
IFNγ+ (% of γδ27+)
Numbers (10⁴)
Numbers (10³)
e
% γδ27- T cells
spleen
Naïve LN
dLN
tumour
f
% γδ T cells
g
Tumour Size (mm³)
h
% γδ T cells
i
SFD
HFD
IL-17
IFNγ
30.9
3.0
60.2
5.9
66.0
0.0
34.0
0.0
% IL-17+ (of γδ27- T cells)
% IFN-γ+ (of γδ27+ T cells)
j
Tumor
Number/mm³
ns
k
γδ17 T cells
- CLC
+ CLC
47.5
71.3
CD3
Ki-67
% Ki67 (of γδ17)
CLC :
l
PBS
γδ17 - CLC
γδ17 + CLC
m
Tumour weight (g)
n
Tumour volume (mm³)
PBS
γδ17 - CLC
γδ17 + CLC
days

Figure 7

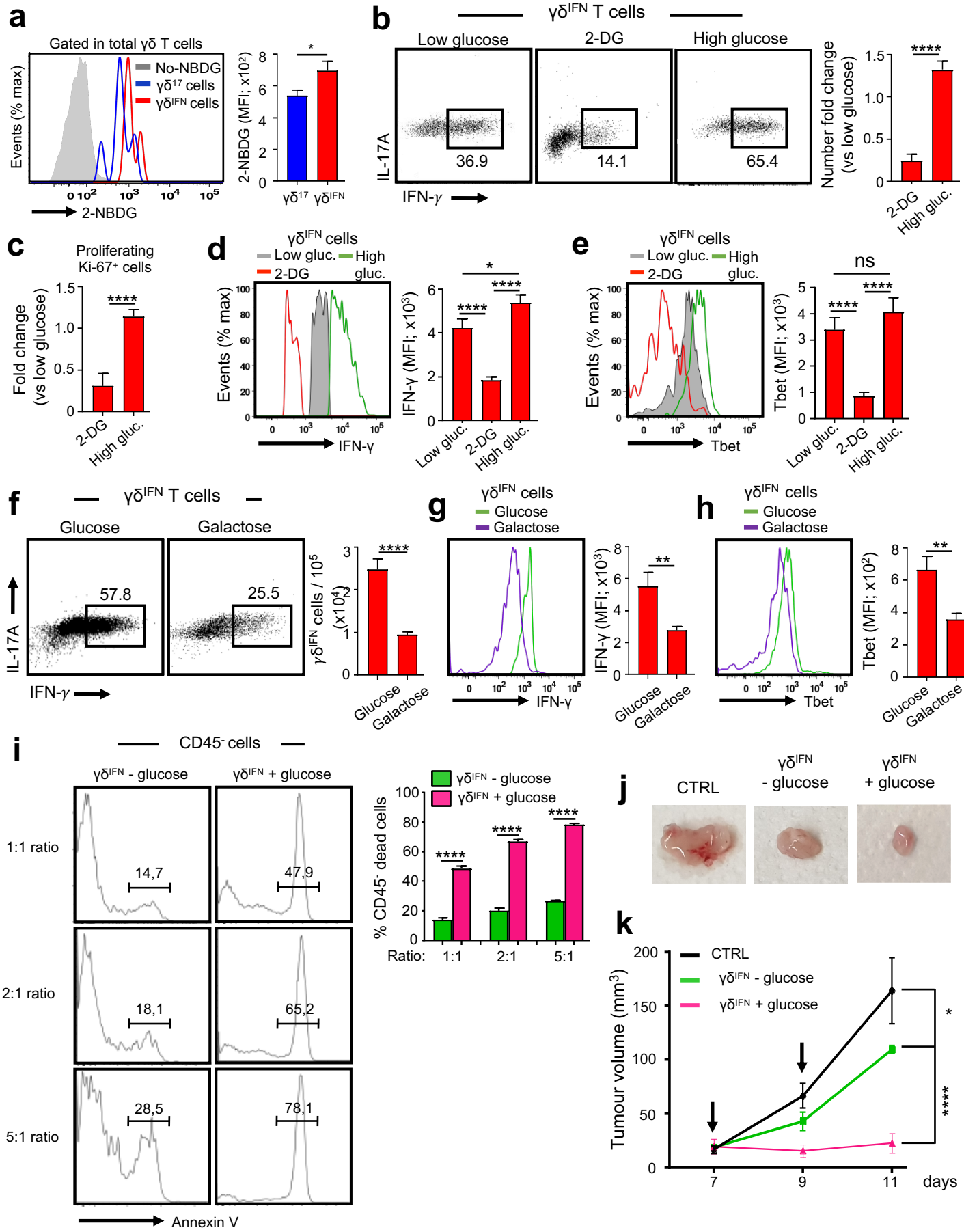
a
Gated in total γδ T cells
No-NBDG
γδ17 cells
γδIFN cells
Events (% max)
2-NBDG
2-NBDG (MFI; x10²)
γδ17
γδIFN
b
γδIFN T cells
Low glucose
2-DG
High glucose
IL-17A
IFN-γ
36.9
14.1
65.4
Number fold change (vs low glucose)
2-DG
High gluc.
c
Proliferating Ki-67+ cells
Fold change (vs low glucose)
d
γδIFN cells
Low gluc.
High gluc.
2-DG
Events (% max)
IFN-γ
IFN-γ (MFI; x10³)
e
Tbet
Tbet (MFI; x10³)
ns
f
Glucose
Galactose
57.8
25.5
γδIFN cells / 10⁵ (x10⁴)
g
h
i
CD45- cells
γδIFN - glucose
γδIFN + glucose
1:1 ratio
2:1 ratio
5:1 ratio
14,7
47,9
18,1
65,2
28,5
78,1
Annexin V
% CD45- dead cells
Ratio: 1:1 2:1 5:1
j
CTRL
k
Tumour volume (mm³)
days

Supplementary Figure 1

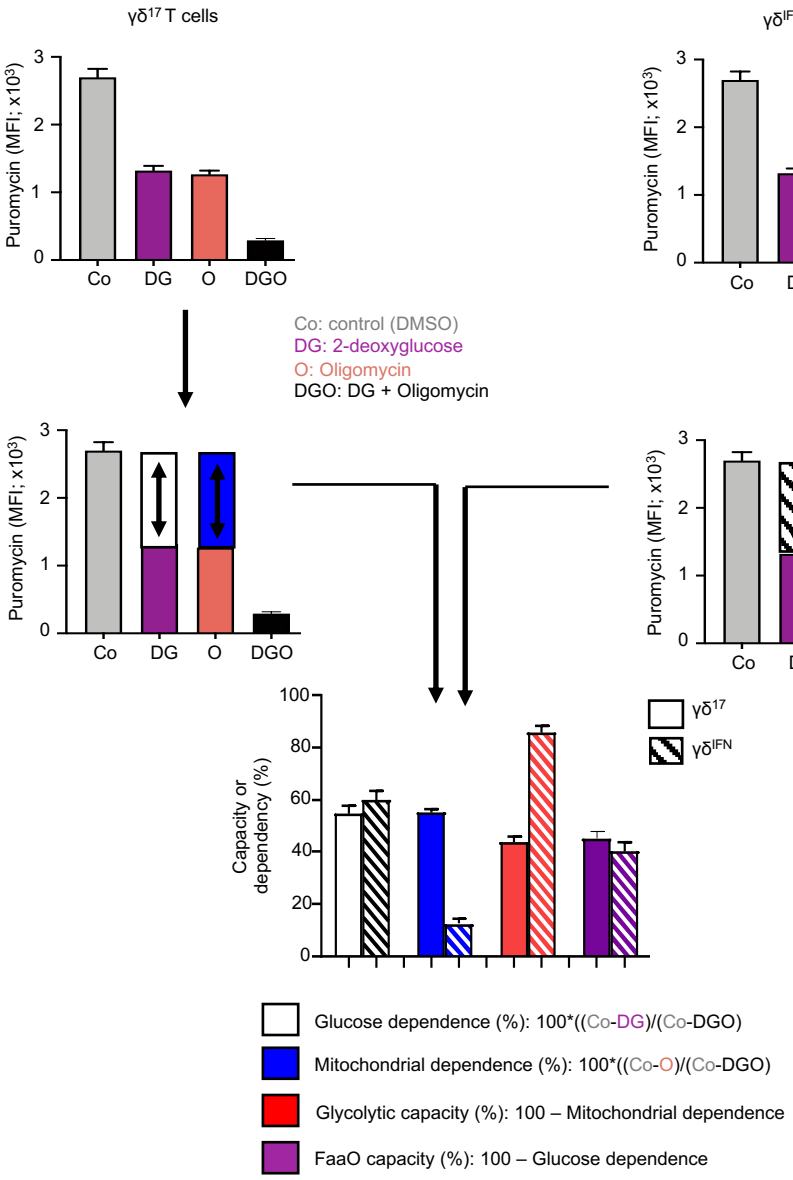

Supplementary Figure 1: SCENITH™ methodology for analysis of cell metabolism. SCENITH™ assesses the impact of metabolic inhibitors on protein synthesis. Mean fluorescence intensity (MFI) of Puromycin is analysed in each condition (Co: control-no inhibition ; DG: 2-deoxyglucose inhibiting glycolysis ; O: oligomycin inhibiting OxPhos and DGO: DG+O inhibitors). Bottom graph shows glucose dependence (white), mitochondrial dependence (blue), glycolytic capacity (red), and fatty acid and amino acid oxidation capacity (purple), which are calculated as detailed in the Methods.

Supplementary Figure 2

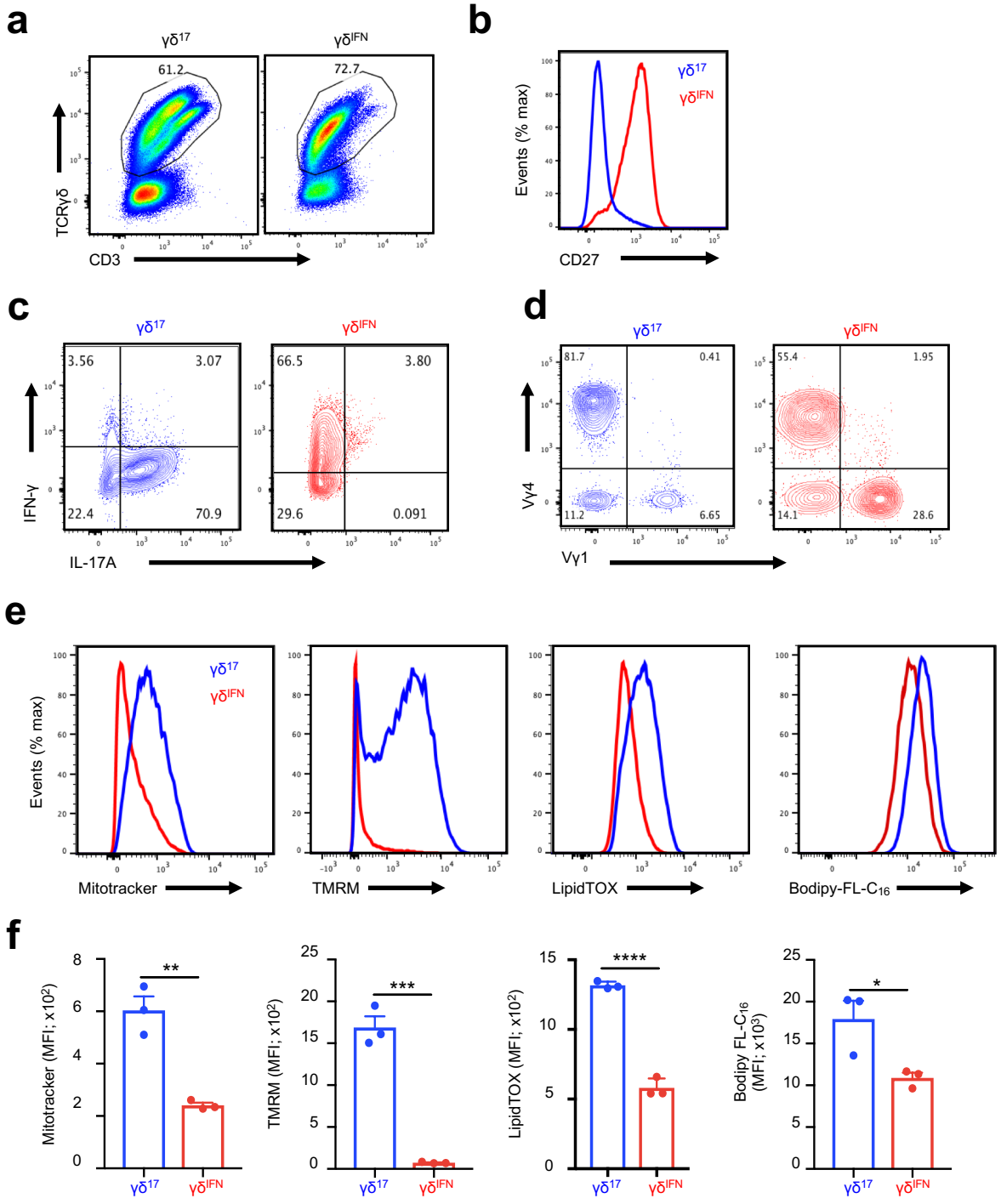

Supplementary Figure 2: γδ^{17} and γδ^{IFN} cells expanded *in vitro* retain their mitochondrial and lipid phenotypes. (a) Representative flow plots of CD3 and TCRδ expression on γδ^{17} and γδ^{IFN} cells expanded *in vitro* from total spleen/LN cells. **(b)** CD27 expression on *in vitro* expanded γδ^{17} and γδ^{IFN} cells. **(c)** IL-17 and IFNγ production by *in vitro* expanded γδ^{17} and γδ^{IFN} cells respectively, following activation with PMA/ionomycin. **(d)** Vγ1 and Vγ4 expression on γδ^{17} and γδ^{IFN} cells expanded *in vitro*. **(e)** Representative staining of γδ^{17} and γδ^{IFN} cells expanded *in vitro* for mitotracker, TMRM, lipidTOX and Bodipy-FL-C_{16}. **(f)** MFI of mitotracker, TMRM, lipidTOX and Bodipy-FL-C_{16} staining on γδ^{17} and γδ^{IFN} cells expanded *in vitro*. n=3, data representative of 3 independent experiments. Error bars show mean + SD, **p < 0.01, ***p<0.001, ****p < 0.0001, using unpaired Student's t-test.

Supplementary Figure 3

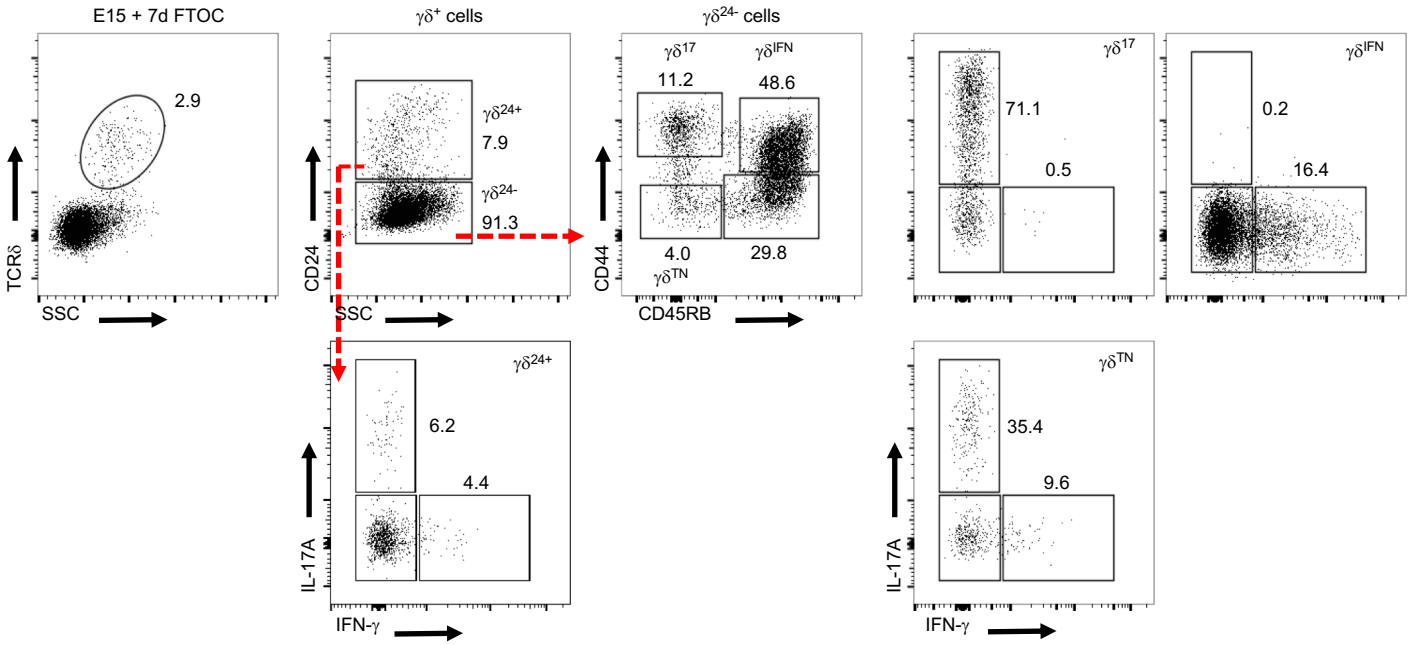

Supplementary Figure 3: γδ^{TN} cells can generate γδ^{17} and γδ^{IFN} cells. Flow cytometry profiles of thymic γδ T cells from E15 thymic lobes that had been cultured for 7-days in fetal thymic organ culture (E15 + 7d FTOC). CD24^{+} (γδ^{24+}) precursors downregulate CD24 to become a CD24^{-}CD44^{-}CD45RB^{-} (γδ^{TN}) population. γδ^{TN} cells are able to become either IL-17-secreting CD44^{hi}CD45RB^{-} γδ^{17} cells, or IFN-γ-producing CD44^{+}CD45RB^{+} γδ^{IFN} cells.

Supplementary Figure 4

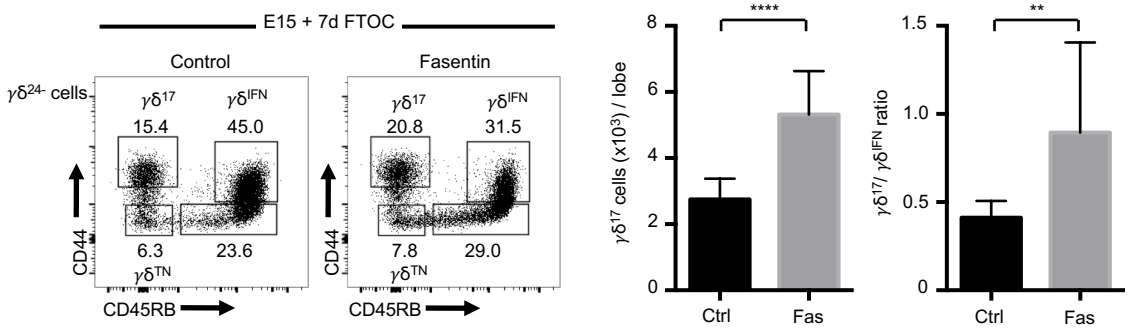

Supplementary Figure 4: Thymic γδ^{17} cells are increased upon inhibition of glucose uptake. Flow cytometry profiles of thymic CD24^{-} γδ T cells further gated as γδ^{TN} (CD44^{-} CD45RB^{-}), γδ^{17} (CD44^{hi}CD45RB^{-}) and γδ^{IFN} (CD44^{+}CD45RB^{+}) cells from E15 thymic lobes in 7-day FTOC with media containing (or not) Fasentin. Histograms show the number of γδ^{17} cells and γδ^{17}/γδ^{IFN} ratio. Data are representative of 2 independent experiments (at least 4 lobes pooled per group per experiment). Error bars show mean ± SEM, $^{**}p < 0.01$, $^{****}p < 0.0001$, using unpaired Student's t-test.

Supplementary Figure 5

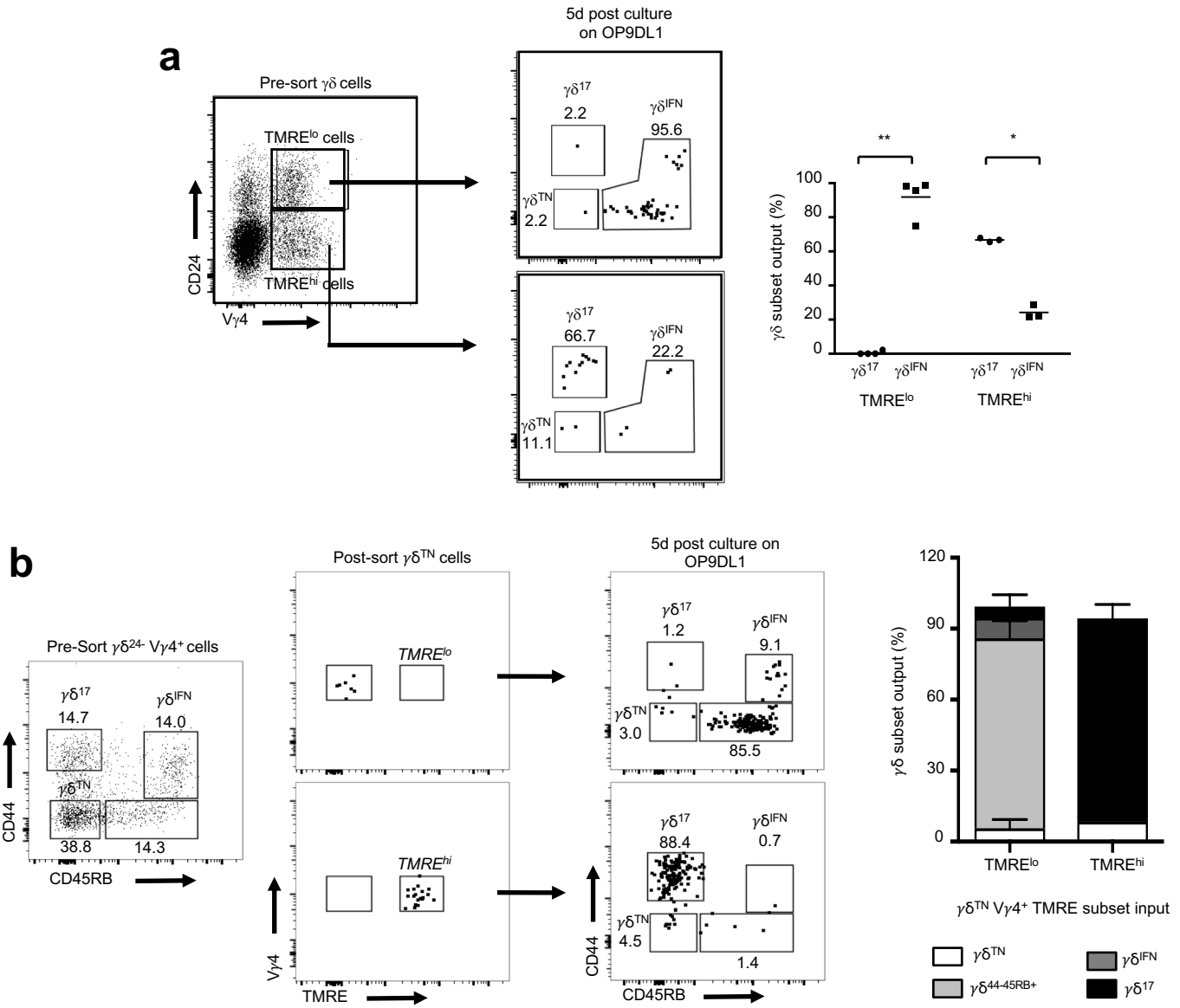

Supplementary Figure 5: Mitochondrial activity identifies Vγ4$^+$ progenitors with distinct effector fates at very early stages. (a) Flow cytometry profiles and percentage of thymic γδ^{17} and γδ^{IFN} cell output from post-sorted TMRE^{lo} and TMRE^{hi} Vγ4$^+$γδ^{24+} cells after 5 days of culture on OP9DL1. Data are representative of 3 independent experiments (cells sorted from n=4 mice pooled per group per experiment). **(b)** Flow cytometry profiles for sorted TMRE^{hi} and TMRE^{lo} Vγ4$^+$γδ^{24+} cells (left) that were then cultured on OP9-DL1 cells for a further 5-days (right plots). Histogram shows the percentage cell output from sorted γδ^{TN}Vγ4$^+$ TMRE hi/lo input. Data are representative of 2 independent experiments (at least 4 lobes pooled per group per experiment).

Supplementary Figure 6

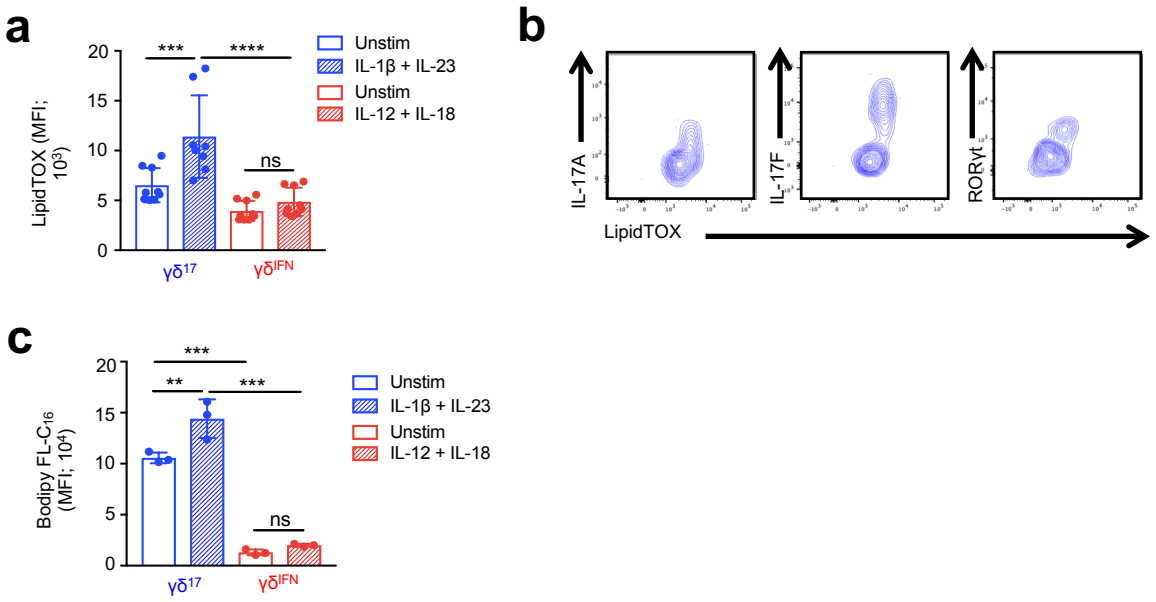

Supplementary Figure 6. Enriched lipid metabolism and higher lipid uptake in γδ^{17} cells. **(a-b)** Feature plots of OxPhos-related **(a)** or lipid-related **(b)** genes from single-cell RNA sequencing of adipose γδ T cells. Cell clusters based on CD27 expression. **(c)** LipidTOX MFI in γδ^{17} (CD27^{-}) and γδ^{IFN} (CD27^{+}) cells from LN cells activated *in vitro* with IL-1β+IL-23 and IL-12+IL-18 respectively. n=9, data pooled from 3 independent experiments. **(d)** Representative plots of LipidTOX staining and IL-17A, IL-17F or RORγt expression in γδ^{27-} cells from LNs activated *in vitro* with IL-1β+IL-23 for 6h. Data representative of 3 independent experiments. **(e)** Bodipy-FL-C_{16} MFI in γδ^{17} (CD27^{-}) and γδ^{IFN} (CD27^{+}) cells unstimulated or stimulated *in vitro* with IL-12+IL-18 or IL-1β+IL-23.(n=3, data from 1 experiment). Error bars show mean + SD, **p < 0.01, ***p < 0.001, ****p < 0.0001 using one-way ANOVA.

Supplementary Figure 7

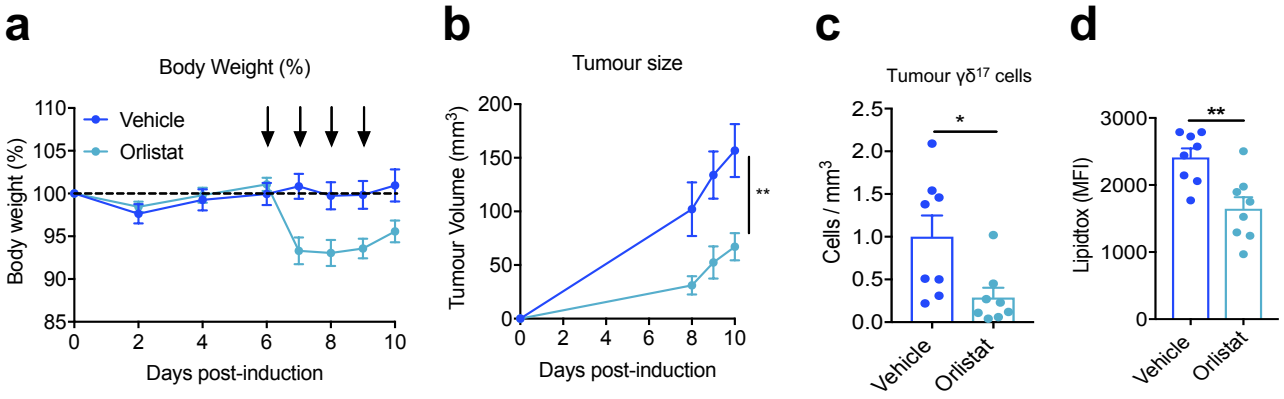

Inhibition of dietary fat uptake reduces tumour growth and γδ^{17} cells in the tumour. B16F10-tumour bearing mice were given daily injections of either vehicle or orlistat on days 6-9, and tumours were analysed on day 10. **(a)** Percentage body weight following tumour cell injection; arrows indicate when orlistat or vehicle were administered. **(b)** Tumour volume on days 8-10 following B16F10 inoculation. Absolute numbers **(c)** and lipidTOX staining **(d)** of tumour-infiltrating γδ^{17} cells on day 10. n=8, data from 1 experiment.

Supplementary Figure 8

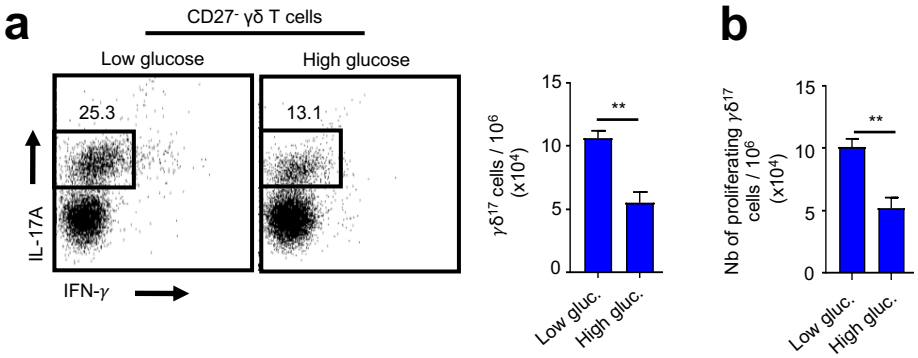

Glucose supplementation diminishes γδ^{17} cell numbers and proliferation. (a) Flow cytometry profiles of peripheral γδ^{17} T cells cultured with media containing low (5mM) or high (50mM) doses of glucose. Graph depicts total numbers of γδ^{17} T cells. **(b)** Number of proliferating Ki-67^{+} γδ^{17} T cells cultured with low or high glucose. Data are representative of three independent experiments (n =3-5 mice per group and per experiment). Error bars show mean ± SEM, **p < 0.01, using unpaired Student's t-test.